

Assessing the performance
of two new acoustic imaging
techniques

D. Nijhof

Assessing the performance of two new acoustic imaging techniques

MSc Thesis

by

Daniëlle Nijhof

to obtain the degree of

Master of Science
in Aerospace Engineering

Control and Operations
Aircraft Noise and Climate Effects

at the Delft University of Technology,
to be defended on Thursday January 25, 2018 at 14:00

Thesis committee:

Prof. Dr. Dick. G. Simons <i>Chair holder</i>	Aircraft Noise and Climate Effects, Delft University of Technology.
Dr. ir. Mirjam Snellen <i>Academic supervisor</i>	Associate Professor, Aircraft Noise and Climate Effects, Delft University of Technology.
Dr. ir. Pieter Sijtsma <i>Industry supervisor</i>	Company owner & researcher, PSA3.
Dr. ir. Sander Hartjes <i>Independent member</i>	Assistant Professor, Air Transport Operations, Delft University of Technology.

An electronic version of this thesis is available at <http://repository.tudelft.nl/>.

"Mathematics. Rightly viewed.
Possesses not only truth, but supreme beauty
– a beauty cold and austere.
Without the gorgeous trappings of paintings or music."

- Bertrand Russell -

Preface

Congratulations! You made it to the preface of my Master thesis report. The report in your hands is the result of nine months of research in the field of acoustics. I am proud of what I achieved during that time and I want to thank everyone who has, to a greater or lesser degree, been involved in my thesis research.

The search for a thesis project started early. Because I was still studying for six months at the Technical University of Lisbon, I had ample time to choose the perfect graduation project for me. On September 20, 2016 I contacted Prof. dr. D.G. Simons about the graduation opportunities in his research group. Consequently I made an appointment with Dr. ir. M. Snellen to talk about a research project on new acoustic imaging techniques.

It immediately clicked between Mirjam and me. I quickly realized that she was passionate about this project and I love her way of communicating: short and businesslike. Because the project is about new techniques, nobody had any clue about the research results. This is also the case with Dr. ir. P. Sijtsma, who is researching aeroacoustic measurements at his company PSA3. Because of his years of experience with acoustic imaging techniques, he has become an expert in this field, which is why he is the perfect industry supervisor.

First of all, I would like to thank Mirjam. For her positive energy, attention and dedication in this project. For her focus on details, the 22 progress meetings and the numerous emails to clarify topics in the field of acoustics to me. With her bird's-eye view, Mirjam has a clear idea of the essence of this project. Many thanks go to Pieter. For his fresh perspective from the industry, for making the link between my research and the performance of other acoustic imaging techniques and for his motivational feedback. I would like to thank Dick for being my graduation professor. Together with Mirjam, he taught the course 'Advanced Aircraft Noise Modeling and Measurement' and introduced the principles of acoustic imaging techniques to me. As luck would have it we are both physics enthusiasts whom somehow ended up in aerospace engineering. Then I would like to thank Roberto. As a cheerful PhD-supervisor, he always had the time to explain something, such as the theory behind a point source or the essence of frequency analysis. My second PhD-supervisor is Anwar, to whom also thanks. He has recorded the six experimental data sets used in this project in the anechoic room of the Faculty of Applied Physics. He also gave me insight into the potential of applying global optimization techniques to acoustics. I would like to thank Lisette for making me feel at home at the ANCE department and guiding me through the paperwork of the thesis process. Then thanks a thousand times to Arianne, Ellen, Hans, Roos and Willemijn. Together you saved me weeks of Matlab run-time and made it possible that the results of this research are so many and so complete. A big thanks goes to Jette for designing the beautiful cover page of this report. Lastly I would like to thank Timothy, the love of my life. For being the solid pillar with whom I could laugh and cry for the victories and vicissitudes of this project. And, not to forget, for introducing me to pyramid writing principles.

This project started on February 13, 2017. And now we are here, at the project conclusion. People sometimes say that you only learn when you make mistakes and ask questions. I made many mistakes and asked many questions. It has been a great time, thanks everyone!

Daniëlle Nijhof
Delft, December 2017

Executive Summary

These are exciting times to work in the field of acoustic imaging: researchers have a more granular understanding of sound than ever before due to the ability to acquire, store, and analyze unprecedented amounts of acoustical data. Therefore the field stands at the advent of new advanced acoustic imaging techniques. This research compared two new acoustic imaging techniques - global optimization and source power integration - and contributes actionable findings for both practitioners and researchers.

First, this research concludes that global optimization is superior compared to other acoustic imaging techniques in locating and quantifying acoustic sources below the Rayleigh limit. This is both true from a spacing as frequency perspective. Second, this research concludes that source power integration identifies source auto-powers for distributed sources more accurately and computationally more efficient than other acoustic imaging techniques.

Acoustic imaging locates and quantifies noise. If noise can be measured it can be reduced.

Field practitioners want to reduce noise. Quantification and localization of noise sources is a prerequisite for noise reduction. To this end, practitioners are well advised to prefer global optimization when trying to identify low frequency sound and/or closely spaced sound sources. Further, practitioners with identified source locations should opt to use source power integration for both its accuracy and efficiency.

Researchers want to further optimize acoustic imaging techniques. Given the promising results of these new techniques thus far, this report recommends researchers in the field of acoustic imaging to test these two techniques under additional circumstances. For example, it would be interesting to investigate the performance of source power integration with experimental data of distributed sources. Further, thus far global optimization was only tested on source data with source conditions which also could be located and quantified by acoustic imaging techniques that need a predefined scan grid. Testing global optimization under circumstances that align with its unique strength - namely the presence of multiple sound sources across three dimensions - would add value. If global optimization passes this test, this would negate the need to predefine, and consecutively scan, multiple two-dimensional scan grids. This would bring the field of acoustic imaging one step closer to the ultimate goal of real-time acoustic imaging across three dimensions.

Contents

Executive Summary	vii
1 Introduction	1
1.1 Acoustic imaging techniques	1
1.2 Research objective and goals	1
1.3 Research structure	1
2 Background of acoustic imaging	3
2.1 Wavelength, frequency, phase.	3
2.2 Discrete Fourier transform	3
2.3 Coherence	4
2.4 Sound Pressure Level and Overall Sound Pressure Level	4
2.5 Signal to Noise Ratio	4
2.6 Conventional beamforming.	5
2.7 Rayleigh limit	7
2.8 DAMAS	7
2.9 Global optimization.	8
2.10 Source Power Integration	11
2.10.1 SPI point.	11
2.10.2 SPI grid	12
2.10.3 Inverse SPI.	13
3 Data sets considered	15
3.1 Point source simulations	15
3.2 Distributed source simulations	16
3.3 Experimental data sets	17
4 Results: point source simulations	19
5 Results: distributed source simulations	25
6 Investigating the performance of GO in identifying closely spaced sound sources	35
7 The two new acoustic imaging techniques applied to experimental data	39
8 Conclusions and recommendations	49
8.1 Conclusions.	49
8.2 Recommendations	50
Bibliography	51
A Other beamforming methods	55
B DAMAS assumptions	57

Nomenclature and abbreviations

Abbreviations

CB	Conventional Beamforming
CMF	Covariance Matrix Fitting
CSM	Cross Spectral Matrix
DAMAS	Deconvolution Approach for the Mapping of Acoustic Sources
DE	Differential Evolution
DL	Diagonal Loading
FB	Functional Beamforming
GA	Genetic Algorithm
GO	Global Optimization
OB	Orthogonal Beamforming
OSPL	Overall Sound Pressure Level
PSF	Point Spread Function
RAB	Robus Adative Beamforming
SNR	Signal to Noise Ratio
SOI	Signal Of Interest
SPI	Source Power Integration
SPL	Sound Pressure Level

Nomenclature

α	iteration index
β	frequency index
\mathbf{C}	Cross Spectral Matrix
\mathbf{C}_{meas}	measured Cross Spectral Matrix
$\mathbf{C}_{\text{model}}$	modeled Cross Spectral Matrix
\mathbf{d}	descendent population member
\mathbf{g}_0	steering vector towards reference point source
\mathbf{m}	candidate solution vector
\mathbf{p}	pressure vector
\mathbf{s}	partner population member
\mathbf{w}	weight vector

\mathbf{x}_{ref}	reference point vector
\mathbf{x}_n	microphone vector of the n -th microphone
$\boldsymbol{\xi}_j$	grid point vector of the j -th grid point
Δt	time difference
γ	generation index
λ	wavelength of sound wave
μ	integration grid index
Ψ	Point Spread Function
$\tilde{\mathbf{C}}$	Cross Spectral Matrix
$\tilde{\mathbf{g}}$	steering vector element without decay part
$\tilde{\mathbf{m}}$	candidate solution vector
\tilde{A}_{ref}	correction factor
\tilde{M}	number of integration grids
$\tilde{p}_{n,m}$	sampled acoustic pressure measured by the n -th microphone
A	source auto-power
a	complex pressure amplitude at the source
B	source auto-power
b	realization from the uniform distribution, ranging from 0 to 1
c	speed of sound
D	array aperture
E_{Bartlett}	Bartlett processor energy function value
E_{CSM}	CSM energy function value
F	positive scalar multiplication factor
f	frequency
g	steering vector element
H	number of sources
h	source index
i	$\sqrt{-1}$
J	cost function
l	block index
M	number of samples during one time period
N	number of microphones
n	microphone index
N_{runs}	number of runs

N_G	number of generations
p_0	reference pressure of $2 \cdot 10^{-5}$ [Pa]
p_{eff}	effective pressure
p_{max}	maximum pressure
p_C	crossover probability, scalar between 0 and 1
p_n	complex pressure amplitude at the n -th microphone
q	population size
R	Rayleigh limit
r	member index
r_1, r_2, r_3, r_4	mutually exclusive member of a population
R_{ref}	distance between the center of the integration grid and the reference point
t	time
u	parameter index
Z	distance between the microphone array plane and the source plane
*	complex conjugate transposition

Introduction

Sound sources are everywhere around us. Although sound in the form of music can be very pleasant to hear, one would rather suppress the sound of aircraft fly-overs [7, 30, 44] or wind turbines [31]. Unwanted sound sources are referred to as noise and the first step in diminishing noise sources is knowing the source locations and strengths. In case of multiple sources, source mapping is an essential element.

1.1. Acoustic imaging techniques

This project is about acoustic imaging techniques, i.e. making source locations and strengths visible. Several acoustic imaging techniques exist, each technique with its own strengths and shortcomings. Conventional Beamforming (CB) [34] is seen as the most robust acoustic imaging technique. With CB multiple microphones record the sound of the source to be mapped and via scanning a region of interest, the source map is computed. However robust, the shortcomings of CB are limited resolution, the presence of side lobes (i.e. high beamforming output levels compared to the main lobe level, without the presence of a source) and the incorrect Sound Pressure Level (SPL) computation for distributed sources. To overcome the limitations of CB, more state-of-the-art acoustic imaging techniques have been developed, for example Functional Beamforming (FB) [16, 17] and the CLEAN-methods [2, 24]. Some of the new acoustic imaging techniques improve on the shortcomings of CB by first computing the CB source map and then altering the obtained map, while other techniques skip the formation of the CB source map in the first place and compute the source map in another manner.

1.2. Research objective and goals

The objective of this research is to assess the performance of two new acoustic imaging techniques, Global Optimization (GO) and Source Power Integration (SPI), by developing algorithms for both techniques, applying them to simulations and experimental data and comparing their performance against two more established acoustic imaging techniques, i.e. CB and the Deconvolution Approach for the Mapping of Acoustic Sources (DAMAS) [40]. These four acoustic imaging techniques will be applied to simulations and six experimental data sets, which defines the scope of this project.

1.3. Research structure

The basic principles of sound and acoustic imaging techniques will be explained in Chapter 2, elaborating on the mathematical representation of CB, DAMAS, GO and SPI. Chapter 3 gives an overview of the data sets on which the algorithms have been applied. As the data sets are subdivided into simulations considering a number of separate sources, simulations considering distributed sources and experimental data, so are the results. The results of the simulations considering a number of separate sources are discussed in Chapter 4, of the simulations considering distributed sources in Chapter 5 and of the experimental data in Chapter 7. Since for GO the model of the received signals can fully reflect the actual situation, it is expected that GO is able to accurately identify closely spaced sound sources. The study of the performance of GO on this issue is described in Chapter 6. Lastly, the conclusions and recommendations are discussed in Chapter 8.

2

Background of acoustic imaging

Sound is a pressure disturbance propagating through a medium (i.e. air or water) as a wave [3]. Although sound can be experienced as pleasant, think of classical music concerts or singing birds, unwanted sound (wind turbine, aircraft flyover) is gathered under the term noise.

In the early days of acoustic imaging, use was made of acoustical mirrors [28, 29]. Elliptical shaped mirrors direct the acoustical rays from a focal point of interest to a microphone. Moving the mirror in small steps enabled the scanning of several focal points, yielding an image of the object of interest. With the increase of computing power and storage space, computational acoustic imaging methods originated [4–12] applying electronic steering. The four acoustic imaging techniques that are part of the scope of this research will be discussed in detail; Conventional Beamforming in Section 2.6, the DAMAS in Section 2.8, Global Optimization in Section 2.9 and Source Power Integration in Section 2.10. A brief overview of six other well-known acoustic imaging techniques is found in Appendix A.

2.1. Wavelength, frequency, phase

Every acoustic signal can be modeled as a sum of sinusoidal waves. To gain understanding of acoustic signals these sinusoidal waves are considered, constituting a signal at a certain frequency. The wavelength is the length of one wave, measured in [m], i.e. the distance travelled in one cycle before the wave repeats itself. The frequency of the wave expresses the number of wave cycles per second. Wavelength, frequency and speed of sound are linked via Equation 2.1.

$$\lambda = \frac{c}{f} \quad (2.1)$$

In Equation 2.1, λ is the wavelength in [m], c is the speed of sound in [m/s] and f is the frequency in [Hz]. Mathematically one wavelength corresponds to 360 degrees or 2π radians. The time delay between two sinusoidal waves can thus be expressed as a phase delay between 0 and 360 degrees. The two sinusoidal waves in Figure 2.1 have a 90-degree phase difference, or 0.5π radians. Both waves have a frequency of 2 Hz, i.e. 2 wave cycles per second.

2.2. Discrete Fourier transform

Acoustic imaging is generally performed in the frequency domain. To go from the time - to the frequency domain, the discrete Fourier transform is applied [34]. According to what is mentioned above, the time signal is considered to be build up from a series of signals at a specific frequency. Let $\tilde{p}_n(t)$ be the pressure measured by the n -th microphone in the time domain, which is discretised to $\tilde{p}_{n,m}$, where m denotes the sample index. The complex pressure amplitudes in the frequency domain at the n -th microphone $p_n(f_\beta)$ are calculated for a block of M samples with the discrete Fourier transform as:

$$p_n(f_\beta) = \frac{2}{M} \sum_{m=1}^M \tilde{p}_{n,m} e^{-2\pi i f_\beta m \Delta t} \quad (2.2)$$

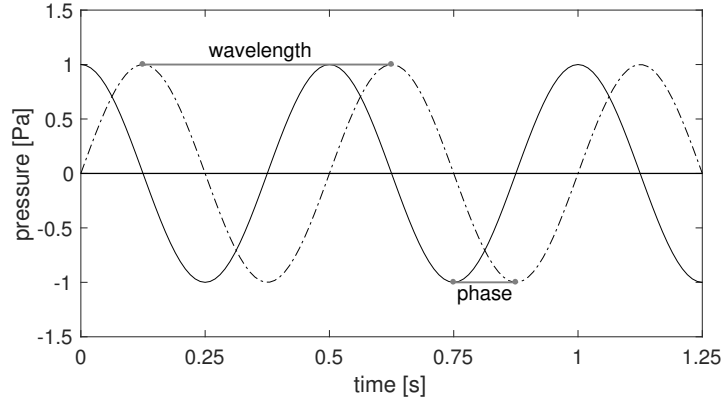


Figure 2.1: Wavelength, frequency and phase visualization.

In Equation 2.2 $p_n(f)$ is the complex pressure amplitude at the n -th microphone in [Pa], n is the microphone index, β is the frequency index, M is the number of samples acquired (block size), $\tilde{p}_{n,m}$ is the sampled acoustic pressure measured by the n -th microphone in [Pa], $i = \sqrt{-1}$ and Δt is the sample interval in [s].

Generally M is a large number of samples. The larger the number of samples in the time domain, the smaller the spacing in the frequency domain:

$$f_\beta = \frac{\beta}{M\Delta t} \quad \beta = 1 \dots \frac{M}{2} - 1 \quad (2.3)$$

2.3. Coherence

Two sound waves are coherent if having equal waveforms (i.e. a sine waveform) and if there exist a constant phase difference between the waves [3]. Loss of coherence [34] happens when sound waves are distorted by turbulent media, i.e. air streams. Sound waves are deformed by the medium they travel through, whereby their phase is different from that in an undisturbed medium.

2.4. Sound Pressure Level and Overall Sound Pressure Level

The Sound Pressure Level (SPL) is a logarithmic measure of the ratio between the effective pressure of a signal and the reference pressure:

$$SPL = 20^{10} \log \left(\frac{p_{\text{eff}}}{p_0} \right) \quad (2.4)$$

In Equation 2.4, SPL is the Sound Pressure Level in [dB], p_{eff} is the effective pressure of the signal in [Pa], defined as the maximum pressure p_{max} divided by $\sqrt{2}$, and p_0 is the reference pressure of $2 \cdot 10^{-5}$ [Pa]. In general, SPL is measured at a certain distance from the sound source. When this report refers to 'a source of 60 dB', it is meant that the source has a SPL of 60 dB at a distance of 1 m from the source.

When multiple sources are present, the SPL can be calculated for each individual source. If one wants to know the Sound Power Level that is caused by all incoherent sound sources together, one calculates the Overall Sound Pressure Level (OSPL):

$$OSPL = 10^{10} \log \sum_{h=1}^H 10^{\frac{SPL(h)}{10}} \quad (2.5)$$

In Equation 2.5, OSPL is the Overall Sound Pressure Level in [dB], $SPL(h)$ is the SPL of the h -th source in [dB], the source index is denoted by h and H is the number of sources.

2.5. Signal to Noise Ratio

The Signal to Noise Ratio (SNR) can be defined as:

$$SNR = 20^{10} \log \left(\frac{p_{\text{eff}}}{p_{\text{eff,noise}}} \right) \quad (2.6)$$

In Equation 2.6, SNR is the Signal to Noise Ratio in [dB] and $p_{\text{eff,noise}}$ is the effective pressure of the noise in [Pa].

2.6. Conventional beamforming

Conventional beamforming (CB)[34] is the simplest and most widely applied beamforming algorithm. A microphone array records sound pressures from one or multiple sources in the time domain, yielding a N -dimensional pressure vector $\tilde{\mathbf{p}}(t)$. The main idea behind CB is to determine for each potential source location the travel time to the various microphones. By delaying the pressures on the microphones to account for the travel times and subsequently summing the delayed signals, the signal originating from the location under consideration is obtained. Therefore CB is often denoted as "delay and sum" beamforming. By using CB in the frequency domain, the delay can be applied by means of a phase multiplication. This results in lower computational times compared to applying CB in the time domain and it yields the possibility to perform frequency analysis. Via Fourier transformation, see Section 2.2, the time domain pressures are converted to complex pressure amplitudes in the frequency domain:

$$\mathbf{p}(f) = \begin{pmatrix} p_1(f) \\ p_2(f) \\ \vdots \\ p_N(f) \end{pmatrix} \quad (2.7)$$

\mathbf{C} is the $N \times N$ -dimensional Cross Spectral Matrix (CSM) and can be calculated by multiplying the pressure vector $\mathbf{p}(f)$ by its complex conjugate. Since experimental data is subject to measurement errors, it is impossible to record $\tilde{\mathbf{p}}(t)$ perfectly. Therefore $\tilde{\mathbf{p}}(t)$ is cut into blocks, with M samples per time block. Suppose $\tilde{\mathbf{p}}(t)$ is cut into L blocks, then $2L - 1$ CSMs are computed for 50% overlapping blocks. The time-averaged CSM is obtained by taking the mean of the CSMs, as expressed in Equation 2.8:

$$\mathbf{C} = \frac{1}{2(2L - 1)} \sum_{l=1}^{2L-1} \mathbf{p}_l \mathbf{p}_l^* \quad (2.8)$$

In Equation 2.8, \mathbf{C} is the CSM, l is the block index and $*$ denotes the complex conjugate transposition.

The microphones are configured on a two-dimensional plane, where the position of microphone n is defined by the vector \mathbf{x}_n . The center of the microphone array is designated as reference point and \mathbf{x}_n points from this reference point towards microphone n . The sound sources to be studied are located on a two-dimensional plane, called the scan plane. The scan plane is generally selected to be parallel to the microphone array plane and the distance between the scan plane and microphone array plane is Z in [m]. The scan plane is discretised in two dimensions, yielding a total number of K grid points. Similar to the microphone locations, the grid points are defined by a vector $\boldsymbol{\xi}_j$, pointing from the reference point, i.e. the center of the microphone array, towards grid point j .

To investigate at which grid points the sound sources are located, one electronically steers from each microphone towards each grid point. The source locations are assumed to be stationary. The steering vector element $g_{j,n}$ is defined between grid point j and microphone n and is expressed in Equation 2.9.

$$g_{j,n} = \frac{1}{\|\mathbf{x}_n - \boldsymbol{\xi}_j\|} e^{-2\pi i f \Delta t_{j,n}} \quad (2.9)$$

In Equation 2.9, $\|\mathbf{x}_n - \boldsymbol{\xi}_j\|$ is the distance between grid point j and microphone n in [m] and $\Delta t_{j,n}$ is the time needed for the sound pressure to travel from grid point j towards microphone n in [s]. Note, the time delay can be calculated by $\Delta t_{j,n} = \|\mathbf{x}_n - \boldsymbol{\xi}_j\|/c$ where c is the speed of sound in [m/s]. The first part of Equation 2.9 is called the 'decay' part, which describes the sound attenuation, i.e. the degree of energy loss of sound propagation in the medium [3]. The second part of Equation 2.9 is called the 'delay' part, which determines the phase relation between the sound sources and microphones. When the level variations between the microphones are small and one wants to only measure the phase variations over the microphone array, the 'decay' part is omitted and the steering vector element $\tilde{g}_{j,n}$ is used:

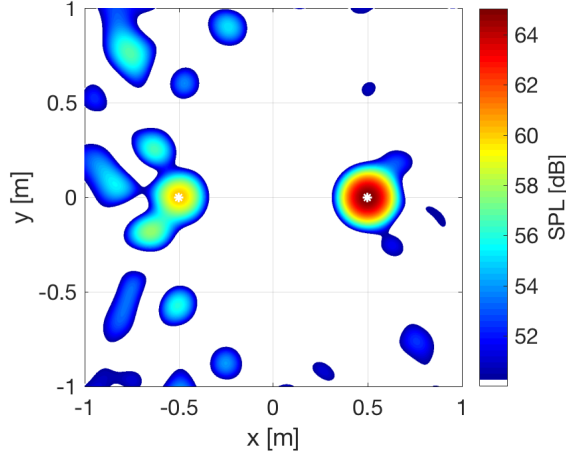


Figure 2.2: CB plot of two point sources of $f = 3000$ Hz. The point source at $(x,y,z) = (-0.5,0,3)$ has a SPL of 60 dB and the point source at $(x,y,z) = (0.5,0,3)$ has a SPL of 65 dB. The white stars represent the point source locations. The used microphone array can be seen in the left plot of Figure 3.1.

$$\tilde{g}_{j,n} = e^{-2\pi i f \Delta t_{j,n}} \quad (2.10)$$

$g_{j,n}$ from Equation 2.9 yields a complex number for each combination of grid point j and microphone n . The N -dimensional steering vector $\mathbf{g}_j(f)$ contains the $g_{j,n}$ values for microphones $n = 1 \dots N$. With the knowledge of the measured pressure amplitudes and phases at the microphone locations via the complex pressure vector $\mathbf{p}(f)$, the complex pressure amplitudes a_j of sound sources located in ξ_j are estimated through minimization of:

$$J_j = \|\mathbf{p} - a_j \mathbf{g}_j\|^2 \quad (2.11)$$

In Equation 2.11, J_j is the cost function [-] and a_j is the complex pressure amplitude in grid point j in [Pa]. $a_j \mathbf{g}_j$ represents the model and the vector \mathbf{p} is constructed from measurements. The objective of CB is to find the complex pressure amplitudes a_j that minimize the difference between the model $a_j \mathbf{g}_j$ and the measurements \mathbf{p} . The solution for a_j is [34]:

$$a_j = \frac{\mathbf{g}_j^* \mathbf{p}}{\|\mathbf{g}_j\|^2} \quad (2.12)$$

One generally considers source auto-powers:

$$B_j = \frac{1}{2} |a_j|^2 = \frac{1}{2} a_j a_j^* = \frac{1}{2} \frac{\mathbf{g}_j^* \mathbf{p}}{\|\mathbf{g}_j\|^2} \left[\frac{\mathbf{g}_j^* \mathbf{p}}{\|\mathbf{g}_j\|^2} \right]^* = \frac{1}{2} \frac{\mathbf{g}_j^* \mathbf{p} \mathbf{p}^* \mathbf{g}_j}{\|\mathbf{g}_j\|^4} = \frac{\mathbf{g}_j^* \mathbf{C} \mathbf{g}_j}{\|\mathbf{g}_j\|^4} \quad (2.13)$$

Equation 2.13 yields the source auto-power in $[\text{Pa}^2]$ for each grid point j . The source auto-powers can be converted from $[\text{Pa}^2]$ to a SPL in [dB] with Equation 2.4. Doing so for all grid points $j = 1 \dots K$ of the scan plane, one obtains a two-dimensional source map. The source map displays for each grid point the estimate for the source auto-power. The resulting source map is called a beamform plot. Since each beamform plot is constructed for a specific frequency, CB can be repeated to obtain beamform plots for multiple frequencies. To get an idea of what a CB plot looks like, see Figure 2.2.

The advantages of CB are simplicity and robustness, i.e. the method requires little computational power in comparison to other acoustic imaging methods and can operate under a variety of conditions. The limitations of this method are low dynamic range (the difference in decibels between the main lobe and the highest side lobe [14]) and array spatial resolution (see Section 2.7), as well as the high number of side lobes, especially at high frequencies [3].

2.7. Rayleigh limit

There is a distance limit at which sound sources can be located from each other and still be recognized as separate sound sources. This limit is called the Rayleigh limit [3] and it is expressed as:

$$R = 1.22 \frac{cZ}{Df} \quad (2.14)$$

In Equation 2.14, R is the Rayleigh limit in [m], Z is the distance between the microphone array plane and the source plane in [m] and D is the array aperture in [m].

To visually explain what the Rayleigh limit involves, two point sources are placed at three different distances from each other: above, on and below the Rayleigh limit. With $Z = 3$ m, $D = 2$ m and $f = 3000$ Hz, the Rayleigh limit is 0.63 m, see Equation 2.14. As one can see in Figure 2.3, the two point sources are clearly visible in the left plot and can no longer be distinguished from each other in the right plot. In the center plot the two point sources are placed at a distance equal to the Rayleigh limit from each other, and one can no longer say with certainty whether there are one source or two sources present.

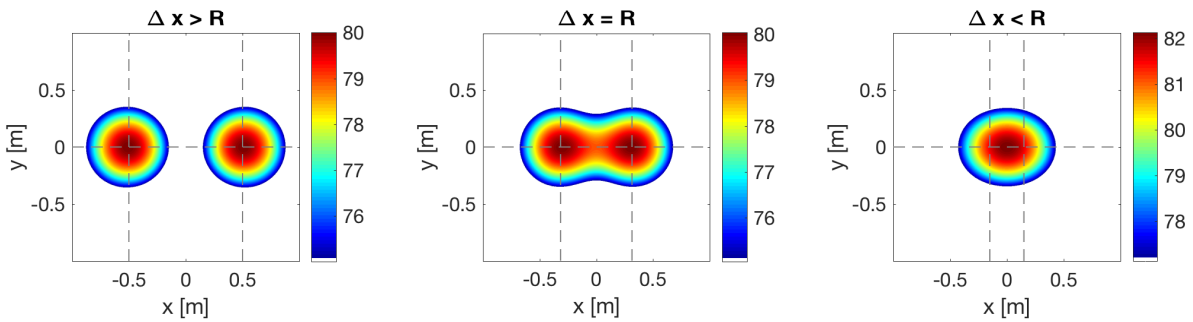


Figure 2.3: Rayleigh limit visualization. Two point sources are placed at three different distances from each other: above, on and below the Rayleigh limit. Left: Above the Rayleigh limit, as $\Delta x = 100$ cm. Center: On the Rayleigh limit, as $\Delta x = 63$ cm. Right: Below the Rayleigh limit, as $\Delta x = 30$ cm.

2.8. DAMAS

DAMAS [40] is developed by NASA in 2004. DAMAS assumes, in contrast to CB, that several sound sources are present. CB uses a model for one source and scans each grid point to quantify the source auto-power. DAMAS uses a model that accounts for the presence of multiple sources and assumes a source to be present at each grid point. The source auto-powers are determined by solving an inverse problem.

From CB one calculates the source auto-powers B_j for grid points $j = 1 \dots K$ via Equation 2.13. DAMAS assumes for each grid point $k = 1 \dots K$ a source to be present with source auto-power A_k in [Pa²]. Since the CSM is calculated from averaged complex pressure vectors, see Equation 2.8, the modeled CSM can be expressed as:

$$\tilde{\mathbf{C}} = \sum_{k=1}^K A_k \mathbf{g}_k \mathbf{g}_k^* \quad (2.15)$$

The reason why the CSM expression for DAMAS is different than for CB in Equation 2.8 is explained in Appendix B. In Equation 2.15, A_k is the source auto-power in [Pa²] at grid point k and \mathbf{g}_k is the N -dimensional steering vector [-] towards grid point k . Combining Equations 2.13 and 2.15 yields:

$$B_j = \frac{\mathbf{g}_j^* \tilde{\mathbf{C}} \mathbf{g}_j}{\|\mathbf{g}_j\|^4} = \frac{\mathbf{g}_j^* \sum_{k=1}^K A_k \mathbf{g}_k \mathbf{g}_k^* \mathbf{g}_j}{\|\mathbf{g}_j\|^4} = \sum_{k=1}^K \frac{\mathbf{g}_j^* \mathbf{g}_k \mathbf{g}_k^* \mathbf{g}_j}{\|\mathbf{g}_j\|^4} A_k = \sum_{k=1}^K \Psi_{j,k} A_k \quad (2.16)$$

Equation 2.16 describes the CB output (B_j) as the result of the presence of K sources. Ψ [-] is the Point Spread Function (PSF) [15]. The objective of DAMAS is to find the source auto-powers A_k for grid points $k = 1 \dots K$. Since source auto-powers in [Pa²] must be positive values, the constraint is included that $A_k \geq 0$.

Equation 2.16 is solved for A_k using the Gauss Seidel procedure. The first step is to rewrite Equation 2.16:

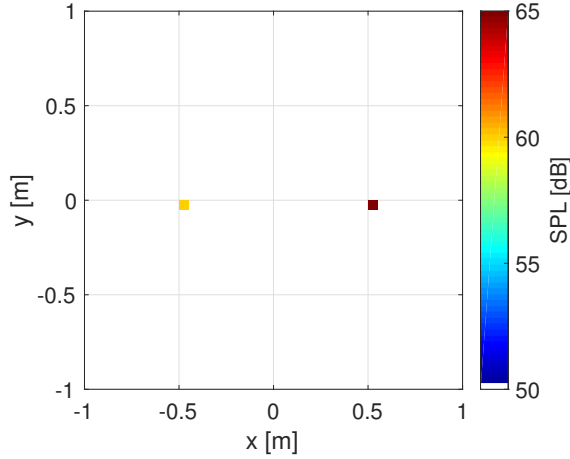


Figure 2.4: DAMAS plot of two point sources of $f = 3000$ Hz. The point source at $(x,y,z) = (-0.5,0,3)$ has a SPL of 60 dB and the point source at $(x,y,z) = (0.5,0,3)$ has a SPL of 65 dB. The used microphone array can be seen in the left plot of Figure 3.1.

$$B_j = \sum_{k=1}^{j-1} \Psi_{j,k} A_k^{(\alpha)} + \Psi_{j,j} A_j^{(\alpha)} + \sum_{k=j+1}^K \Psi_{j,k} A_k^{(\alpha-1)} \quad (2.17)$$

In Equation 2.17, α indicates the iteration number and $\Psi_{j,j} = 1$. The second step is to rearrange Equation 2.17 to obtain an expression for $A_j^{(\alpha)}$:

$$A_j^{(\alpha)} = B_j - \sum_{k=1}^{j-1} \Psi_{j,k} A_k^{(\alpha)} - \sum_{k=j+1}^K \Psi_{j,k} A_k^{(\alpha-1)} \quad (2.18)$$

The third and last step of the Gauss-Seidel procedure is to iteratively solve Equation 2.18. A suitable starting point for the iteration is $A_j^{(\alpha)} = 0$ and one calculates $A_j^{(\alpha)}$ for grid points back and forth, thus $j = 1 \dots K$ and $j = K \dots 1$. As stated earlier, since source auto-powers in $[\text{Pa}^2]$ must be positive values, the constraint is included that $A_j^{(\alpha)} \geq 0$.

After applying the Gauss-Seidel procedure, one obtains the source auto-powers A_j in $[\text{Pa}^2]$ for grid points $j = 1 \dots K$. With Equation 2.4, SPLs in [dB] are calculated and a DAMAS source map is obtained. To get an idea of what a DAMAS plot looks like, see Figure 2.4.

DAMAS is seen as a robust method, since it finds back the actual source auto-powers hidden behind the so-called dirty source map of CB. However, for a total number of K grid points, the PSF has dimensions $K \times K$. This makes DAMAS computationally much more demanding than CB. To speed up each individual iteration and to add regularization by applying a low pass filter, DAMAS2 [41] was developed. In addition, DAMAS3 [41] also has fast iterations and reduces the required number of iterations by applying a Wiener filter. For NASA, the next step was to develop 3D DAMAS [43] in 2005, in order to find source locations and auto-powers in three dimensional space. However, the underlying premises of the DAMAS and 3D DAMAS still are that the noise regions under study are distributions of statistically independent sources. Therefore, DAMAS-C [42] was developed, to permit the identification and quantification of coherent sound sources.

2.9. Global optimization

CB and DAMAS are based upon a scan grid of source locations in two-dimensional space. The global optimization method leaves the concept of calculating the source auto-powers for predefined grid points behind and focuses on finding the actual source locations and auto-powers in a grid-free manner through global optimization. Side lobes obstruct the optimization process, because side lobes are local optima in the energy landscape where the global optimum must be found. Global optimization methods are capable of escaping local optima and famous examples are simulated annealing [26, 27], genetic algorithms (GA) [22, 23, 25] and

ant colony algorithms [18, 19]. The Differential Evolution (DE) method [20, 21] is an algorithm from the genetic algorithms category. The main principle of DE is the mimicking of natural evolution of species according to Charles Darwin [21]. From now on, Differential Evolution as global optimization method is referred to as Global Optimization, GO.

For simulations, the number of sound sources the algorithm should search for is determined with the rank of the CSM, since the number of linearly independent rows or columns of the CSM indicates the number of sound sources present. For experimental data, the number of significantly distinct eigenvalues indicates the number of sound sources the algorithm should search for. Per sound source four parameters have to be found, i.e. the (x,y,z)-coordinates and the source auto-power in [Pa²].

The choice for the energy function is the determining factor whether GO converges to the correct solution or not. GO generates so-called candidate solutions, which are vectors containing trial values for the unknown parameters. The energy function calculates the 'fitness' per candidate solution, i.e. the smaller the difference between the candidate solution and the correct parameter values, the "fitter" is the candidate solution. In this research, two energy functions are considered:

1. Bartlett processor
2. CSM energy function

The Bartlett processor only considers the phase variation of the pressures over the microphones of the array, see Equation 2.8, by taking the inner product between \mathbf{p} en $\tilde{\mathbf{g}}$. The energy value of the Bartlett processor is maximum when the phase variation in \mathbf{p} completely corresponds to the phase variation in $\tilde{\mathbf{g}}$. The CSM energy function is based on the same equation used in deriving the CB expression, Equation 2.11. The CSM energy function thus includes both the phase variation and the amplitude of the source.

The Bartlett processor searches for the (x,y,z)-coordinates of the sound sources, thus there are three unknown parameters per sound source. The trial values for the unknown parameters are merged into a vector \mathbf{m} . In case of two sound sources, $\mathbf{m} = [x1, y1, z1, x2, y2, z2]$. The Bartlett processor exploits the steering vector without the 'decay' part, see Equation 2.10, and is given by:

$$E_{\text{Bartlett}}(\mathbf{m}, f) = - \sum_{h=1}^H [\tilde{\mathbf{g}}_h^*(\mathbf{m}, f) \mathbf{C}_{\text{meas}}(f) \tilde{\mathbf{g}}_h(\mathbf{m}, f)] \quad (2.19)$$

In Equation 2.19, \mathbf{m} is the candidate solution vector and \mathbf{C}_{meas} is the measured CSM. The closer the source location of the candidate solution lies to the true location of the sound source, the greater the match between the steering vector and the measured CSM and the larger the scalar between square brackets in Equation 2.19. The scalars are summed for the number of sound sources H . The minus before the summation sign ensures that candidate solutions closer to the global optimum get assigned a lower energy value E_{Bartlett} , since GO as implementation is such that it is aiming to find the minimum energy.

Exploiting the Bartlett processor as energy function of GO, one obtains the sound source locations, but not the source auto-powers. The auto-power in [Pa²] of source h of solution \mathbf{m} is calculated by using the expression of the CB algorithm. Once one knows the source location, the source auto-power at that location can be calculated with Equation 2.13, where 'grid point j ' is set as the obtained source location.

The second energy function considered is the CSM energy function. The CSM energy function searches for four parameters per sound source, i.e. the (x,y,z)-coordinates and the source auto-power in [Pa²]. For two sound sources, this incorporates $\tilde{\mathbf{m}} = [x1, y1, z1, ap1, x2, y2, z2, ap2]$. The main principle of the CSM energy function is to minimize the difference between the modeled and measured CSM.

The steering vector towards source h of candidate solution $\tilde{\mathbf{m}}$ is calculated with Equation 2.9. Note, the calculation of the steering vector uses the first three elements per sound source h of the candidate solution $\tilde{\mathbf{m}}$, i.e. the (x,y,z)-coordinates. The modeled CSM is calculated with the steering vector and the fourth element per sound source h of the candidate solution. Subsequently the CSM energy function minimizes the difference between the modeled and measured CSM:

$$E_{\text{CSM}}(\tilde{\mathbf{m}}, f) = \sum \sum |\mathbf{C}_{\text{model}}(\tilde{\mathbf{m}}, f) - \mathbf{C}_{\text{meas}}(f)|^2 \quad (2.20)$$

As one can see, the CSM energy function applies least squares minimization between the modeled and measured pressures, and thus takes the same approach as the CB algorithm. In order to obtain a scalar as energy value for the CSM energy function, the double summation in Equation 2.20 sums the $N \times N$ elements. The closer the source of the candidate solution lies to the true sound source (i.e. location and source auto-power), the more the modeled CSM resembles the measured CSM. Therefore, candidate solutions closer to true source locations have a smaller difference between the modeled and measured CSM and thus $E_{\text{CSM}}(\tilde{\mathbf{m}}, f)$ yields a smaller energy value.

Now that one has a way to distinguish between good and less good candidate solutions via the energy functions, the GO algorithm starts. The initial population consists of q randomly chosen parameter value combinations, containing trial values for the unknown parameters. The generation index is γ and the population member index is r , thus $\mathbf{m}_{\gamma,r} = \mathbf{m}_{3,6}$ indicates the sixth candidate solution from the third generation. At each generation, a partner population is calculated from the current population:

$$\mathbf{s}_{\gamma,r_1} = \mathbf{m}_{\gamma,r_2} + F(\mathbf{m}_{\gamma,r_3} - \mathbf{m}_{\gamma,r_4}) \quad (2.21)$$

In Equation 2.21, \mathbf{s}_{γ,r_1} is the r_1 -th partner population member of generation γ , F is a positive scalar multiplication factor and r_1, r_2, r_3, r_4 are integers between 1 and q , mutually exclusive. Mutually exclusive has the effect that $\mathbf{s}_{\gamma,r}$ is calculated from different members $\mathbf{m}_{\gamma,r}$. The higher the value of F is chosen, the greater the difference between the current population and the partner population. Research has shown that F must be set between 0 and 1 for optimal functioning of the algorithm [28].

The next step is to calculate the descendant population from the current population and the partner population. Crossover is applied between $\mathbf{m}_{\gamma,r}$ and $\mathbf{s}_{\gamma,r}$ with probability p_C . The parameters values u of $\mathbf{d}_{\gamma,r}$ are chosen according to:

$$\mathbf{d}_{\gamma,r,u} = \begin{cases} \mathbf{m}_{\gamma,r,u} & \text{if } b \geq p_C \\ \mathbf{s}_{\gamma,r,u} & \text{if } b < p_C \end{cases} \quad (2.22)$$

In Equation 2.22, u is the parameter index, b is a realization from the uniform distribution, ranging from 0 to 1, and p_C is the crossover probability, a scalar between 0 and 1. Equation 2.22 generates q potential descendant population members. Members of the next generation are based upon comparing the members of the descendant population with these of the current population as:

$$\mathbf{m}_{\gamma+1,r} = \begin{cases} \mathbf{d}_{\gamma,r} & \text{if } E(\mathbf{d}_{\gamma,r}) < E(\mathbf{m}_{\gamma,r}) \\ \mathbf{m}_{\gamma,r} & \text{if } E(\mathbf{d}_{\gamma,r}) \geq E(\mathbf{m}_{\gamma,r}) \end{cases} \quad (2.23)$$

Executing Equation 2.23 for all members r in generation γ , one obtains the next generation $\gamma + 1$. This process is repeated N_G times, where N_G denotes the number of generations. A member converges to the global optimum, i.e. the correct parameter values, for decreasing energy values E_{Bartlett} or E_{CSM} . The following five parameters can be set for the DE algorithm [28]:

- q population size
- F multiplication factor
- p_C crossover probability
- N_G number of generations
- N_{runs} number of runs

To get an idea of GO results, see Figure 2.5. Two point sources of $f = 3000$ Hz are placed at $(x,y,z) = (-0.5,0,3)$ with a SPL of 60 dB and at $(x,y,z) = (0.5,0,3)$ with a SPL of 65 dB. GO is applied with $q = 128$, $F = 0.4$, $p_C = 0.75$, $N_G = 500$ and $N_{\text{runs}} = 10$. As one can see, the CSM energy function value decreases over the generations. This is because the measured and modeled CSM increasingly resemble each other. Because the SPLs of the point sources are 60 and 65 dB and the maximum sound pressure p_{max} is adopted in generating the CSM rather than the effective pressure p_{eff} , it is expected that GO finds source auto-powers of $8 \cdot 10^{-4} \text{ Pa}^2$ and $2.5 \cdot 10^{-3} \text{ Pa}^2$, see Equation 2.4. And indeed, GO with the CSM energy function finds the point sources at $(x,y,z) = (-0.5,0,3)$ and $(0.5,0,3)$ with source auto-powers of $8 \cdot 10^{-4} \text{ Pa}^2$ and $2.5 \cdot 10^{-3} \text{ Pa}^2$.

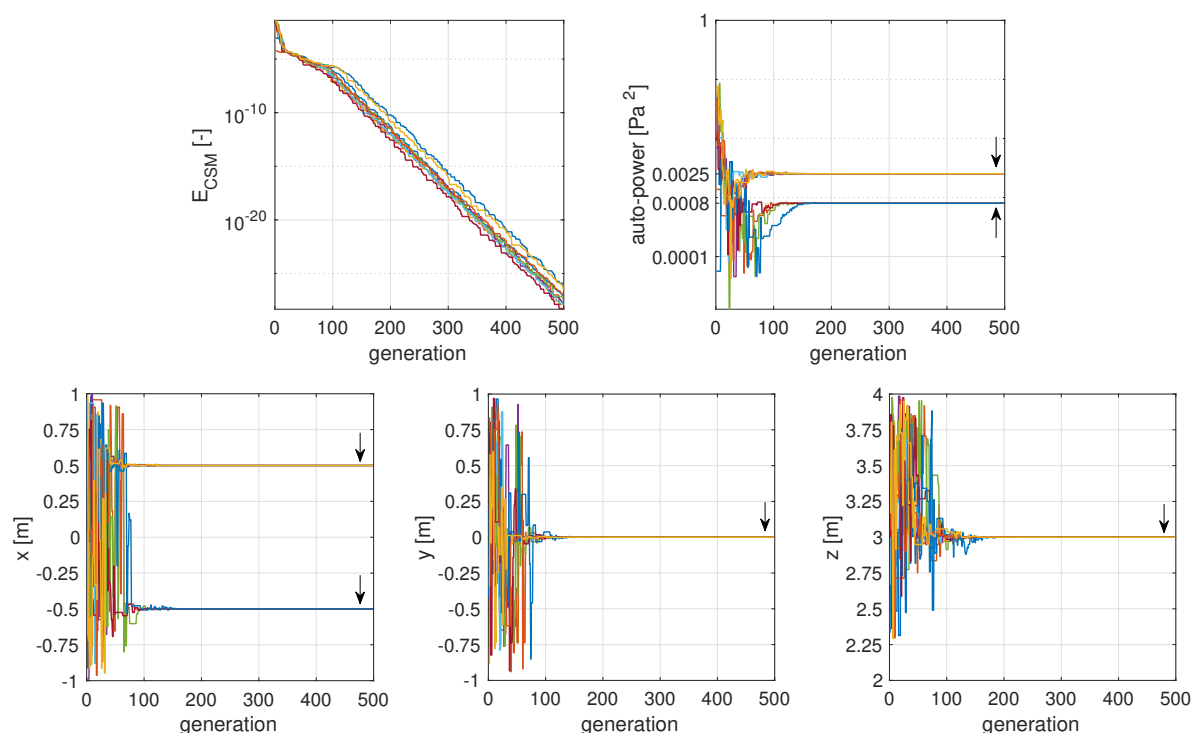


Figure 2.5: GO with the CSM energy function applied to two point sources of $f = 3000$ Hz. The point source at $(x,y,z) = (-0.5,0,3)$ has a SPL of 60 dB and the point source at $(x,y,z) = (0.5,0,3)$ has a SPL of 65 dB. The arrows indicate the results, i.e. within 500 generations the (x,y,z) -coordinates and source-autopowers of the two point sources are accurately determined by GO.

2.10. Source Power Integration

Source Power Integration (SPI) [34] is the newest acoustic imaging technique. The general idea behind SPI is to integrate source auto-powers over an area of interest, to obtain the OSPL for that area, see Equation 2.5.

The hypothesis is that the added value of SPI in comparison to other acoustic imaging techniques lies in the quantification of distributed sources. Correctly quantifying distributed sources ensures that the study of noise reduction is deployed where it is most needed. SPI includes three types:

1. SPI point
2. SPI grid
3. Inverse SPI

The assumption of SPI is that the sound of a certain area is caused by a reference source or by a grid of reference sources. The objective of SPI is to quantify the source auto-power(s) of the reference source(s), such that the match between the sound caused by the reference source(s) most closely resembles the sound that is caused by the real source(s). Depending on the type of noise being studied, one chooses which type of SPI to apply. It is assumed that SPI yields the best results when the reference sources mimic the real sources as accurately as possible.

SPI point is applied when the noise under study is one point source or multiple point sources. SPI grid is applied to distributed sources, thus to multiple closely spaced point sources. For distributed sources with varying source auto-powers, inverse SPI is the best choice. Inverse SPI is able to accurately quantify the source auto-powers of multiple parts of the distributed source. SPI point and SPI grid are generally applied with a threshold to avoid integration over side lobes, and to avoid integration over negative results, in the case of diagonal removal. The three SPI types will be discussed in detail in this section.

2.10.1. SPI point

The fastest and simplest way to apply SPI is by summing the CB results on an integration grid and scaling the summation to one reference point source:

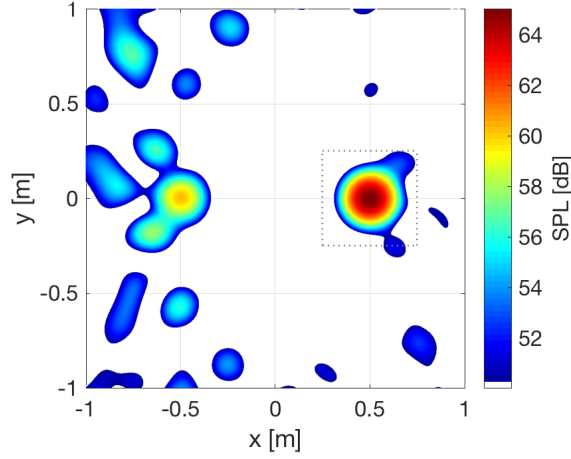


Figure 2.6: SPI point applied to one point source at $(x,y,z) = (0.5,0,3)$ with a SPL of 65 dB. The dotted lines represent the integration grid. The SPI point result is 65.25 dB.

$$SPI = \frac{\sum_{j=1}^K \mathbf{w}_j^* \mathbf{C} \mathbf{w}_j}{\sum_{j=1}^K \mathbf{w}_j^* \mathbf{g}_0 \mathbf{g}_0^* \mathbf{w}_j} \quad (2.24)$$

In Equation 2.24, \mathbf{w}_j is the weight vector [-] of grid point j , defined by $\mathbf{w}_j = \mathbf{g}_j / \|\mathbf{g}_j\|^2$, K is the number of points of the integration grid, \mathbf{C} is the CSM and \mathbf{g}_0 is the steering vector [-] towards the location of the reference point source. Generally, the reference point source is placed in the middle of the integration grid, yet this is not a requirement. In principle one is free in the definition of the integration grid, but SPI loses accuracy in the case of large integration grids. Neighboring grids may affect each other.

To get an idea of SPI, SPI point is applied to a point source at $(x,y,z) = (0.5,0,3)$. The integration grid is plotted in Figure 2.6. The point source has a SPL of 65 dB and the SPI point result is 65.25 dB.

2.10.2. SPI grid

SPI point scales the summed CB results to one reference point source. Instead of scaling by one reference point source, SPI grid scales by a group of incoherent sound sources:

$$SPI = \frac{\sum_{j=1}^K \mathbf{w}_j^* \mathbf{C} \mathbf{w}_j}{\sum_{j=1}^K \mathbf{w}_j^* (\sum_{k=1}^K \mathbf{g}_k \mathbf{g}_k^*) \mathbf{w}_j} \tilde{A}_{\text{ref}} \quad (2.25)$$

Equation 2.25 is basically equal to Equation 2.24, instead that the summed beamforming results are scaled with respect to a group of incoherent point sources located at grid points $k = 1 \dots K$. Because the denominator increases with the number of reference point sources K , the dimensionless correction factor \tilde{A}_{ref} is adopted in Equation 2.25. The correction factor \tilde{A}_{ref} is expressed as:

$$\tilde{A}_{\text{ref}} = \frac{R_{\text{ref}}}{\|\mathbf{x}_{\text{ref}} - \boldsymbol{\xi}_k\|} \sum_{k=1}^K \left| \tilde{\mathbf{g}}_{\mathbf{x}_{\text{ref}}, \boldsymbol{\xi}_k} \right|^2 \quad (2.26)$$

From now on, it is important not to be confused about reference point sources and the reference point. A specific reference point is defined, generally 1 m from the center of the integration grid. In Equation 2.26, R_{ref} is the distance between the center of the integration grid and the reference point (thus when the reference point is defined 1 m from the center of the integration grid, $R_{\text{ref}} = 1$ m), $\|\mathbf{x}_{\text{ref}} - \boldsymbol{\xi}_k\|$ is the distance between the reference point and the reference point source at grid point k and $\tilde{\mathbf{g}}_{\mathbf{x}_{\text{ref}}, \boldsymbol{\xi}_k}$ represent the steering vector element from the reference point to the reference point source at grid point k . Because of \tilde{A}_{ref} , the numerator of Equation 2.25 increases with the same rate as the denominator. In other words, the choice for the number of reference point sources does not affect the SPI result.

Equation 2.25 assumes an equal number of grid points and reference point sources. However, it is also possible to adopt K_g grid points and K_r reference point sources:

$$SPI = \frac{\sum_{j=1}^{K_g} \mathbf{w}_j^* \mathbf{C} \mathbf{w}_j}{\sum_{j=1}^{K_g} \mathbf{w}_j^* \left[\sum_{k=1}^{K_r} \mathbf{g}_k \mathbf{g}_k^* \right] \mathbf{w}_j} \tilde{A}_{\text{ref}} \quad (2.27)$$

2.10.3. Inverse SPI

When the sound source is built from multiple point sources with varying source auto-powers, the stronger sources overshadow the weaker sources. Inverse SPI is able to accurately determine source auto-powers of different parts of the sound source. Inverse SPI extends the principle of Equation 2.25 to multiple subgrids. Where Equation 2.25 assumes that the sound comes from one subgrid, the same principle is extended to multiple subgrids $\mu = 1 \dots \tilde{M}$ to obtain:

$$J = \left\| \mathbf{C} - \sum_{\mu=1}^{\tilde{M}} A_{\mu} \sum_{k=1}^{K_{\mu}} \mathbf{g}_{\mu,k} \mathbf{g}_{\mu,k}^* \right\|^2 \quad (2.28)$$

In Equation 2.28, A_{μ} is the auto-power in $[\text{Pa}^2]$ per reference point source placed at grid point k of integration grid μ . μ is the integration grid index and \tilde{M} is the number of integration grids. K_{μ} does not have to be equal for all μ , i.e. the subgrids can have different sizes. Solving Equation 2.28 for A_{μ} yields a set of \tilde{M} linear equations:

$$\sum_{\mu=1}^{\tilde{M}} \sum_{k=1}^{K_{\mu}} \left(\mathbf{g}_j^* \mathbf{g}_{\mu,k} \mathbf{g}_{\mu,k}^* \mathbf{g}_j \right) A_{\mu} = \mathbf{g}_j^* \mathbf{C} \mathbf{g}_j \quad (2.29)$$

Equation 2.29 can be solved with the constraint $A_{\mu} \geq 0$ similar to DAMAS, with the Gauss-Seidel procedure, see Section 2.8. After solving for A_{μ} , one calculates the correction factors \tilde{A}_{ref} with Equation 2.26 and obtains integrated results through:

$$SPI = A_{\mu} \tilde{A}_{\text{ref}} \quad (2.30)$$

In Equation 2.30, A_{μ} is the auto-power in $[\text{Pa}^2]$ per subgrid μ and \tilde{A}_{ref} is the dimensionless correction factor expressed in Equation 2.26.

3

Data sets considered

The data sets used in this research are subdivided into simulations considering a number of separate sources, simulations considering distributed sources and experimental data. Simulations are imitations of reality. The purpose of using simulations is to see whether the algorithm works, because the expected result is equal to the input. To investigate the effect of having imperfect measurements, noise can be added to simulations. This is done to test the algorithm under suboptimal, but known, conditions.

For the point source - and distributed source simulations, a circular array of 48 microphones is employed, see the left plot in Figure 3.1. The experimental data sets are recorded with an array of 64 microphones with a random distribution, see the right plot in Figure 3.1. When studying the experimental sound pressure data, it became clear that six microphones in the array were defect. The defect microphones are plotted in red. The experimental data sets are thus recorded with 58 microphones. The data sets used in this research are discussed in detail in Sections 3.1 - 3.3.

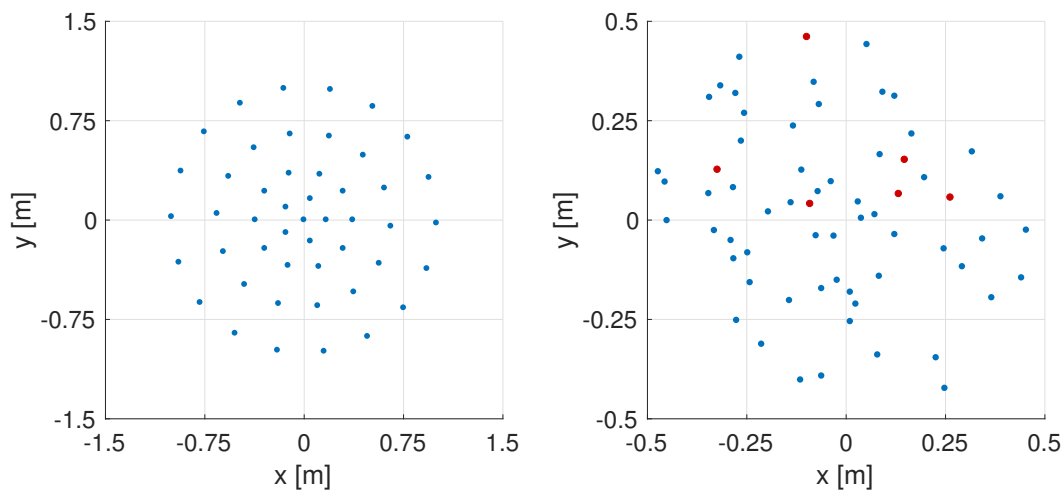


Figure 3.1: Two examples of microphone arrays. Left: Circular array of analytical benchmark case [28], used for the point source - and distributed source simulations. Right: Array with a random distribution of 64 microphones [28], used to record the experimental data sets. The 58 functioning microphones are plotted in blue and the six defect microphones are plotted in red.

3.1. Point source simulations

It is interesting to inspect how the algorithms work for a number of separated sources. The simplest case possible is an individual point source and the degree of difficulty increases with an increased number of point sources. The first point source simulation is one point source placed at $(x,y,z) = (0,0,3)$ with a SPL of 100 dB and $f = 3000$ Hz, see the left plot of Figure 3.2. The second point source simulation consists of two point

sources of the same frequency and different SPLs. The point source of 80 dB is placed at $(x,y,z) = (-0.5,0,3)$ and the point source of 60 dB is placed at $(x,y,z) = (0.5,0,3)$, both $f = 5000$ Hz, see the right plot of Figure 3.2. All algorithms (CB, DAMAS, GO, SPI) are applied to the point source simulations.

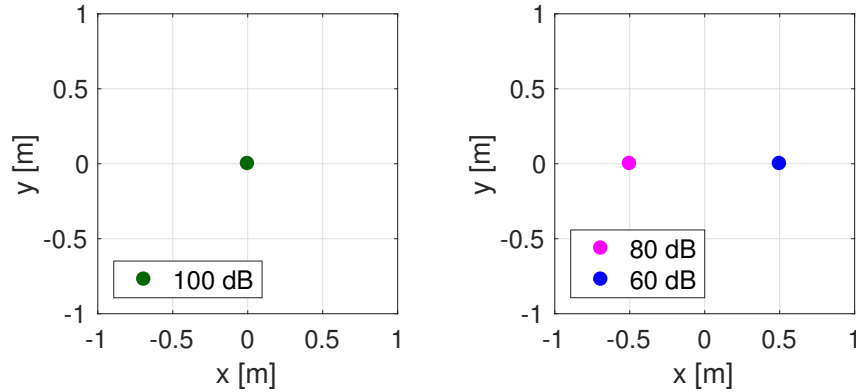


Figure 3.2: Visualization of the point source simulations. Left: One point source at $(x,y,z) = (0,0,3)$ with SPL 100 dB and $f = 3000$ Hz. Right: Two point sources at $(x,y,z) = (-0.5,0,3)$ and $(0.5,0,3)$, SPLs 80 dB and 60 dB, both $f = 5000$ Hz.

3.2. Distributed source simulations

Distributed sources encompass leading/trailing edge noise, i.e. no longer individual points are vibrating. One can think of flow noise or a string in the wind. Distributed sources are simulated by placing large amounts of point sources close together. How close together is close enough? To determine the source spacing to obtain a distributed source, the ratio of two variables must be taken into account, namely the spacing between the point sources and the wavelength of the sources:

$$\lambda \gg d \quad (3.1)$$

In Equation 3.1, d is the spacing between the sources in [m] and λ is the wavelength of the sources in [m]. Two distributed sources are used in this research and both are line sources. Distributed source 1 is a line source built from 100 point sources of 60 dB and $f = 2000$ Hz, with a spacing of 1 cm between the sources, see the left plot of Figure 3.3. With the speed of sound of 343 m/s, one knows from Equation 2.1 that $\lambda = 0.17$ m, thus the requirement posed by Equation 3.1 is fulfilled. To test the performance of inverse SPI, distributed source 2 is a line source built from 99 point sources of $f = 2000$ Hz, divided in three parts of 33 sources, see the right plot of Figure 3.3. In the first part the point sources have a SPL of 60 dB, in the second part 55 dB and in the third part 65 dB. Noise with five different SNRs is added, see Section 2.5, resulting in a total of 12 data sets of distributed sources. CB, DAMAS and SPI are applied to these data sets.

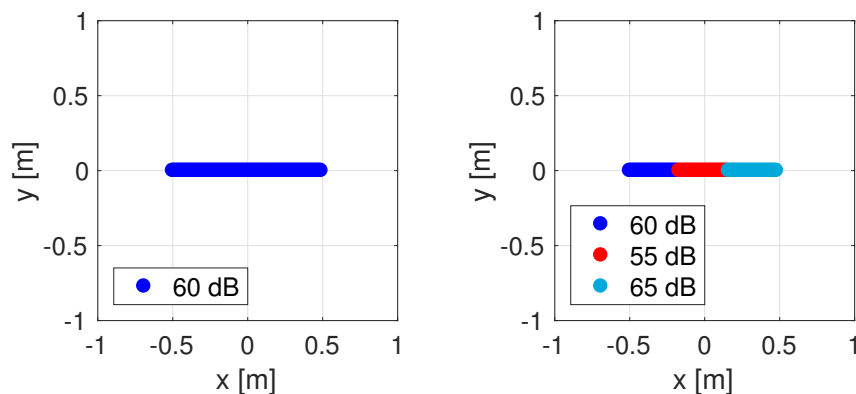


Figure 3.3: Visualization of the distributed source simulations. Left: Line source 1, 100 point sources of 60 dB, $f = 2000$ Hz, spacing 1 cm and array distance of 3 m. Right: Line source 2, 99 point sources, $f = 2000$ Hz, spacing 1 cm and array distance of 3 m. Line source 2 is subdivided in three parts, with SPLs 60 dB, 55 dB and 65 dB.

3.3. Experimental data sets

There are six experimental data sets available for this project, all recorded in the anechoic chamber of the Faculty of Applied Sciences in Delft by Anwar Malgoezar [28]. The acoustic sources for the first experimental data set are two small speakers placed 80 cm apart, broadcasting white noise. The distance from the array plane is 1.87 m and the point in the middle of the speakers is aligned with the array center. The array plane made an angle of 4° with the vertical, which was corrected for in the microphone coordinates. The data are recorded with a sampling frequency of 50 kHz and the sampling time is 60 s. The time-averaged CSMs are obtained by dividing the data set into 6000 blocks of 0.01 s, with 50% overlap between the blocks. In this manner the frequency steps between the consecutive CSMs is $\Delta f = 100$ Hz. The second experimental data set is recorded in the exact same settings as the first, but now only the left speaker broadcasts white noise, i.e. the speaker located at $(x,y,z) = (-0.40,0,1.87)$. And for the third set, only the right speaker broadcasts white noise, i.e. the speaker located at $(x,y,z) = (0.40,0,1.87)$, see Figure 3.4.

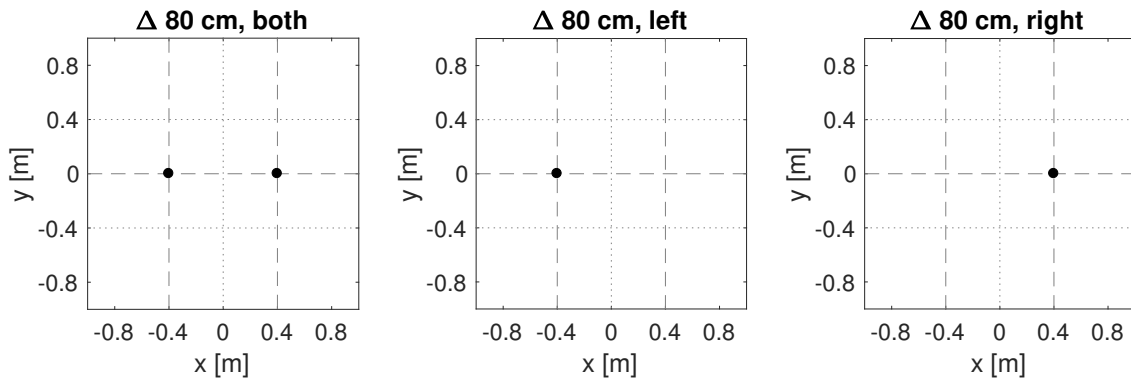


Figure 3.4: Visualization of the experimental data sets. Left: Two speakers placed $\Delta 80$ cm apart, both broadcasting white noise. Center: One speaker at $(x,y,z) = (-0.40,0,1.87)$ broadcasting white noise. Right: One speaker at $(x,y,z) = (0.40,0,1.87)$ broadcasting white noise.

The fourth, fifth and sixth experimental data sets are the same in all aspects as the first three data sets, except that the two speakers are now placed 25 cm apart, see Figure 3.5. All algorithms (CB, DAMAS, GO, SPI) are applied to the experimental data sets.

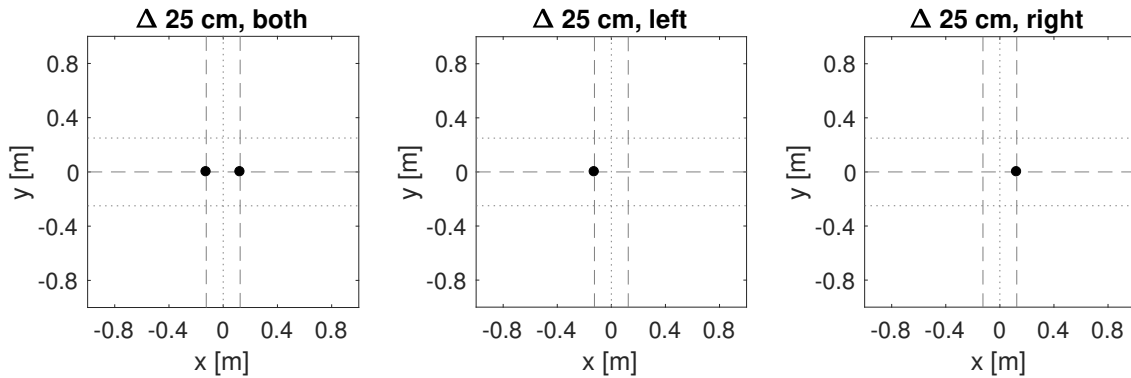


Figure 3.5: Visualization of the experimental data sets. Left: Two speakers placed $\Delta 25$ cm apart, both broadcasting white noise. Center: One speaker at $(x,y,z) = (-0.125,0,1.87)$ broadcasting white noise. Right: One speaker at $(x,y,z) = (0.125,0,1.87)$ broadcasting white noise.

4

Results: point source simulations

As the data sets are subdivided into simulations considering a number of separate sources, simulations considering distributed sources and experimental data, so are the results. The results of the point source simulations are presented in this chapter and the results of the distributed source simulations are presented in Chapter 5. The experimental data results are discussed in Chapter 7. The order of the presentation of the results will be: CB - DAMAS - GO - SPL.

The first point source simulation is one point source of 100 dB and $f = 3000$ Hz, see Section 3.1 and the left plot in Figure 3.2. Applying CB and setting the dynamic range to 24 dB yields the left plot in Figure 4.1. The point source is clearly visible, surrounded by side lobes. Applying DAMAS and setting the dynamic range to 100 dB yields the right plot in Figure 4.1. The point source is clearly visible no side lobes are present.

When GO is applied, one has the choice to use the Bartlett processor or the CSM energy function. With the Bartlett processor, one finds the source location, thus the (x,y,z) -coordinates of the source. The source auto-power is calculated back by using the CB algorithm, see Section 2.9. With the CSM energy function, one finds the source location and auto-power. Both the Bartlett processor and CSM energy function are employed. The algorithm settings for GO are $p_C = 0.75$, $F = 0.40$, $N_{\text{runs}} = 10$, $q = 128$ and $N_G = 100$. The lower and upper bounds are set from -1 to +1 for the x-coordinate and y-coordinate, from 2 to 4 for the z-coordinate and from 0 to 10 for the source auto-power. The latter only applies to the CSM energy function.

Applying GO with the Bartlett processor results in the energy landscape - and convergence plots of Figure 4.2. In order to keep the plots clear, it has been decided to plot only the values belonging to the fittest member per generation, i.e. the member with the lowest energy function value. Energy landscape plots show the energy values of the fittest members per generation on the y-axis and the estimated parameters on the x-axis. Convergence plots show the course of the estimates for the parameters over the generations. Thus the (x,y,z) -coordinates of the fittest members are plotted on the y-axes against generation on the x-axes. Figure 4.2 shows that the point source is found at $(x,y,z) = (0,0,3)$, easily within 100 generations. With the estimated source location, the source auto-power is calculated by applying CB. From the microphone array one steers towards the source location. Applying CB through Equation 2.13 yields a SPL of 100 dB for the point source at $(x,y,z) = (0,0,3)$.

Applying GO with the CSM energy function yields the estimates for four parameters: the (x,y,z) -coordinates and the source auto-power. Where the results of GO with the Bartlett processor consisted of energy landscape - and convergence plots for the (x,y,z) -coordinates, the results of GO with the CSM energy function also include plots for the source auto-power. The results are shown in Figure 4.4. Because the SPL of the point source is 100 dB and the maximum sound pressure p_{max} is adopted in generating the CSM rather than the effective pressure p_{eff} , it is expected that GO finds a source auto-power of 8 Pa^2 , see Equation 2.4. And indeed, GO with the CSM energy function finds the point source at $(x,y,z) = (0,0,3)$ with a source auto-power of 8 Pa^2 .

For SPL, the expected result is the OSPL of the sound source(s). Since the algorithm is applied to one point source, the expectation is to get a result equal to the SPL of this source, 100 dB. Applying SPL point with three different integration grids gives indeed a result of 100 dB. See Figure 4.3 for a visualization of the three employed integration grids.

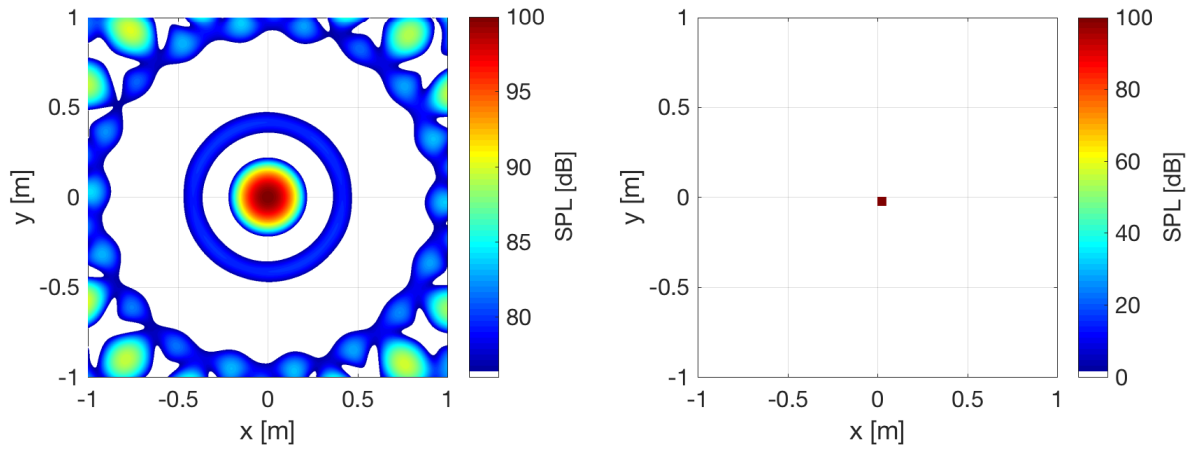


Figure 4.1: One point source of 100 dB and $f = 3000$ Hz. Left: CB. The point source is clearly visible, surrounded by side lobes. Right: DAMAS. The point source is clearly visible and the plot exhibits no side lobes.

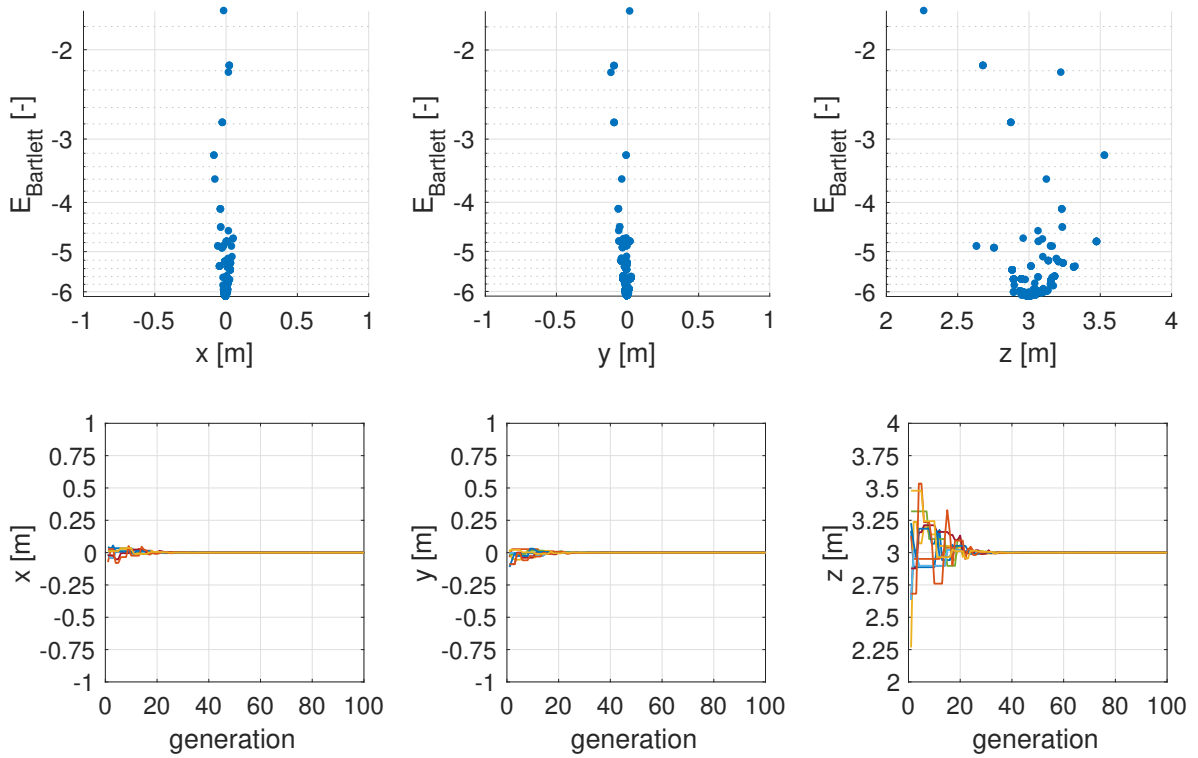


Figure 4.2: GO with the Bartlett processor applied to one point source of 100 dB and $f = 3000$ Hz, placed at $(x,y,z) = (0,0,3)$. The source is easily found within 100 generations.

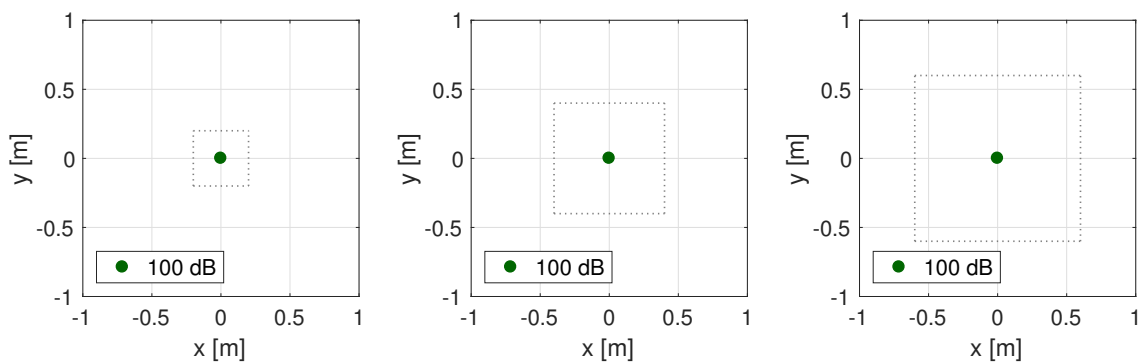


Figure 4.3: Three integration grids for the first point source simulation: one point source placed at $(x,y,z) = (0,0,3)$ with a SPL of 100 dB and $f = 3000$ Hz.

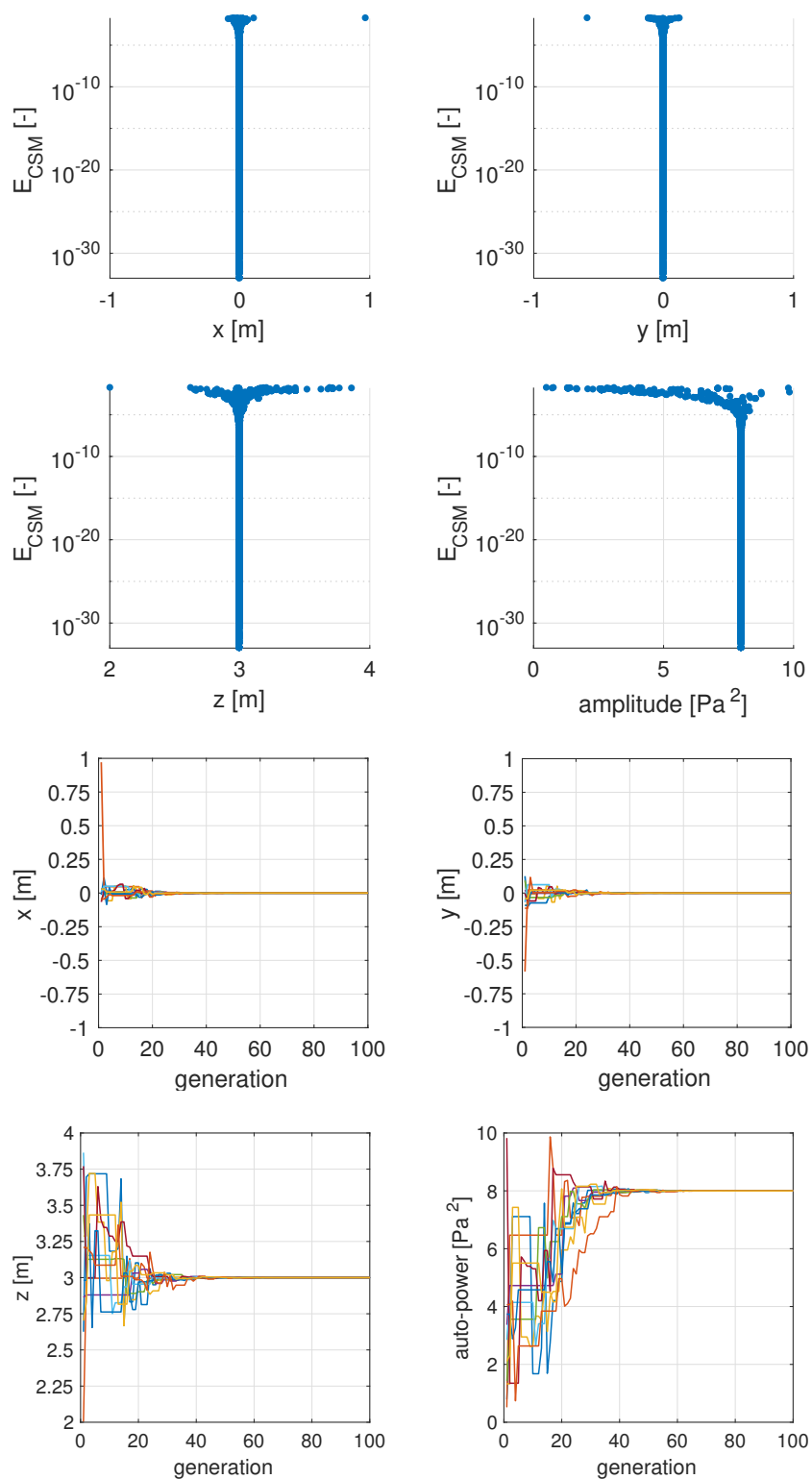


Figure 4.4: Energy landscape and convergence plots of GO with the CSM energy function, applied to one point source of 100 dB and $f = 3000$ Hz, placed at $(x,y,z) = (0,0,3)$.

The second simulation consists of one point source placed at $(x,y,z) = (-0.5,0,3)$ with a SPL of 80 dB and one point source placed at $(x,y,z) = (0.5,0,3)$ with a SPL of 60 dB, both $f = 5000$ Hz, see the right plot of Figure 3.2. Applying CB and setting the dynamic range to 24 dB yields the left plot in Figure 4.5. The 80 dB point source is clearly visible, yet the 60 dB point source is hidden between side lobes. Applying DAMAS and setting the dynamic range to 80 dB yields the right plot in Figure 4.5. Both sources are clearly visible, the plot exhibits no side lobes. DAMAS yields the exact SPLs for both sources: 80 dB and 60 dB.

For GO, both the Bartlett processor and CSM energy function are applied. The algorithm settings for GO are $p_C = 0.75$, $F = 0.40$, $N_{\text{runs}} = 10$, $q = 128$ and $N_G = 500$. Applying GO with the Bartlett processor results in the energy landscape - and convergence plots of Figure 4.6. One source is found at $(x,y,z) = (-0.5,0,3)$, yet the other source at $(x,y,z) = (0.5,0,3)$ is not found. Since only one source location is found, the auto-power of that source can be calculated by applying CB. From the microphone array one steers to the source location and CB yields a SPL of 80.04 dB for the point source at $(x,y,z) = (-0.5,0,3)$.

Applying GO with the CSM energy function results in the energy landscape - and convergence plots of Figure 4.8. Because the SPLs of the point sources are 80 dB and 60 dB, it is expected that GO finds a source auto-power of $8 \cdot 10^{-2} \text{ Pa}^2$ and a source auto-power of $8 \cdot 10^{-4} \text{ Pa}^2$, see Equation 2.4. And indeed, GO with the CSM energy function finds the point sources at $(x,y,z) = (-0.5,0,3)$ and $(0.5,0,3)$ with source auto-powers of $8 \cdot 10^{-2} \text{ Pa}^2$ and $8 \cdot 10^{-4} \text{ Pa}^2$.

For SPI, the expected result is the OSPL value of the point sources. For two point sources of 60 dB and 80 dB, respectively, the expected outcome is thus 80.04 dB. Applying SPI point gives a result of 79.93 dB, i.e. 0.11 dB lower than expected. For a visualization of the integration grid, see the left plot of Figure 4.7. Concerning the integration grid, the size does not have a big effect on the result. Though, one must make sure both sources are included in the integration grid.

Instead of applying SPI point with an integration grid that includes both sources, it can also be applied to one point source at the time. SPI point is applied with integration grids of 10×10 cm around the sources, with a resolution of 1 cm. For a visualization of the integration grids, see the center and right plots in Figure 4.7. This means that two square grid are defined, of which the 80 dB source and 60 dB source, respectively, are the center grid points. The reference points are placed in the middle of the integration grids, i.e. on the 80 dB and 60 dB sources. SPI point yields 80.02 dB for the 80 dB source and 76.97 dB for the 60 dB source. The result for the 80 dB source corresponds well to the actual SPL, yet the result for the 60 dB source is much higher than expected. An explanation could be that the stronger source of 80 dB 'overshadows' the weaker source of 60 dB. The unwanted consequence is that a part of the sound power that is integrated in the grid of the 60 dB source, is caused by the 80 dB source.

Inverse SPI is applied with the same integration grids as SPI point, i.e. grids of 10×10 cm around the sources, with a resolution of 1 cm. Inverse SPI yields 80.57 dB for the 80 dB source and 60.46 dB for the 60 dB source. Although the 80 dB source is now a bit overestimated, the result for the 60 dB source improved a lot compared to the SPI point result. The explanation is that inverse SPI minimizes the difference between the CSM and the two grids simultaneously, whereas SPI point only looks at one grid at the time. The consequence is that the stronger source of 80 dB overshadows the weaker source of 60 dB when SPI point is applied, whereas inverse SPI is able to accurately determine the SPLs of both sound sources.

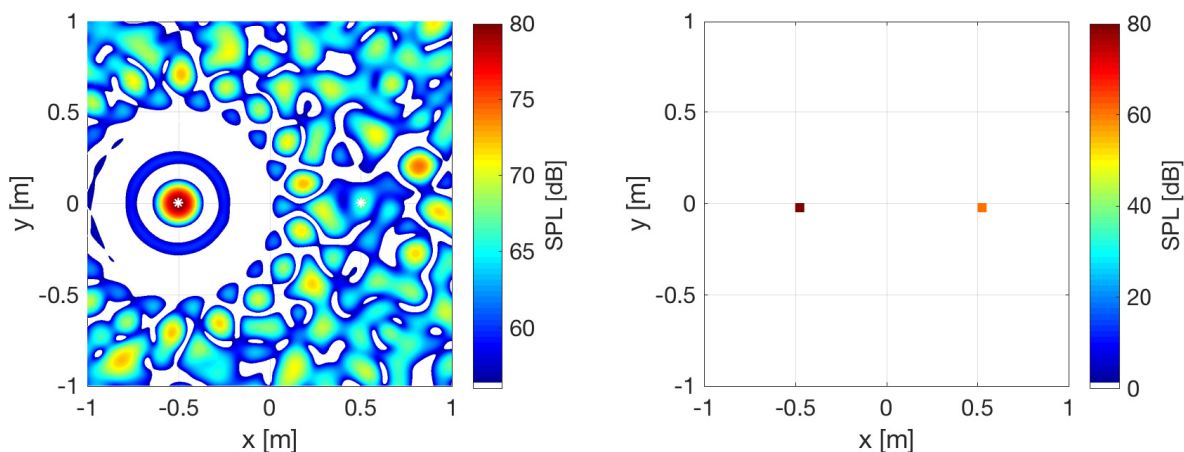


Figure 4.5: Two point sources, placed at $(x,y,z) = (-0.5,0,3)$ with a SPL of 80 dB and placed at $(x,y,z) = (0.5,0,3)$ with a SPL of 60 dB, both $f = 5000$ Hz. Left: CB. The 80 dB point source is clearly visible, yet the 60 dB point source is hidden between side lobes. The white stars indicate the source locations. Right: DAMAS. Both sources are clearly visible, the plot exhibits no side lobes. DAMAS yields the exact SPLs for both sources: 80 dB and 60 dB.

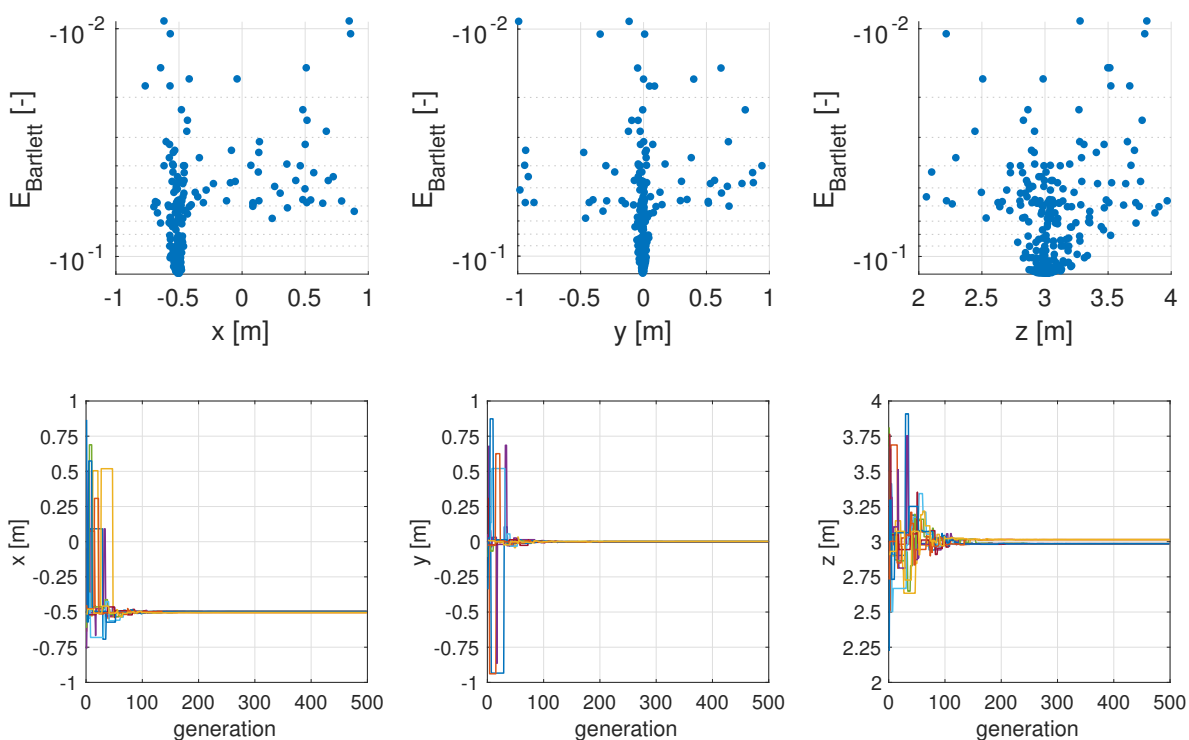


Figure 4.6: GO with the Bartlett processor applied to two point sources, placed at $(x,y,z) = (-0.5,0,3)$ with a SPL of 80 dB and placed at $(x,y,z) = (0.5,0,3)$ with a SPL of 60 dB, both $f = 5000$ Hz. One source is found at $(-0.5,0,3)$, yet the other source is not found.

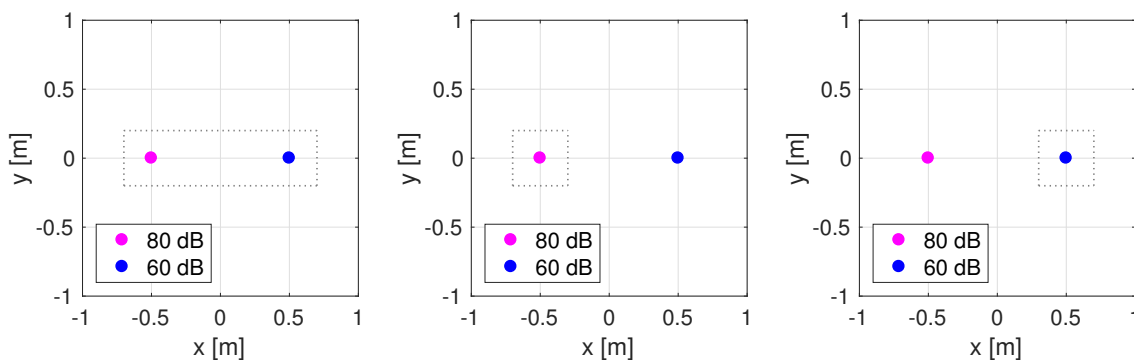


Figure 4.7: Three integration grids for the second point source simulation: one point source of 80 dB placed at $(x,y,z) = (-0.5,0,3)$ and one point source of 60 dB placed at $(x,y,z) = (0.5,0,3)$, both $f = 5000$ Hz.

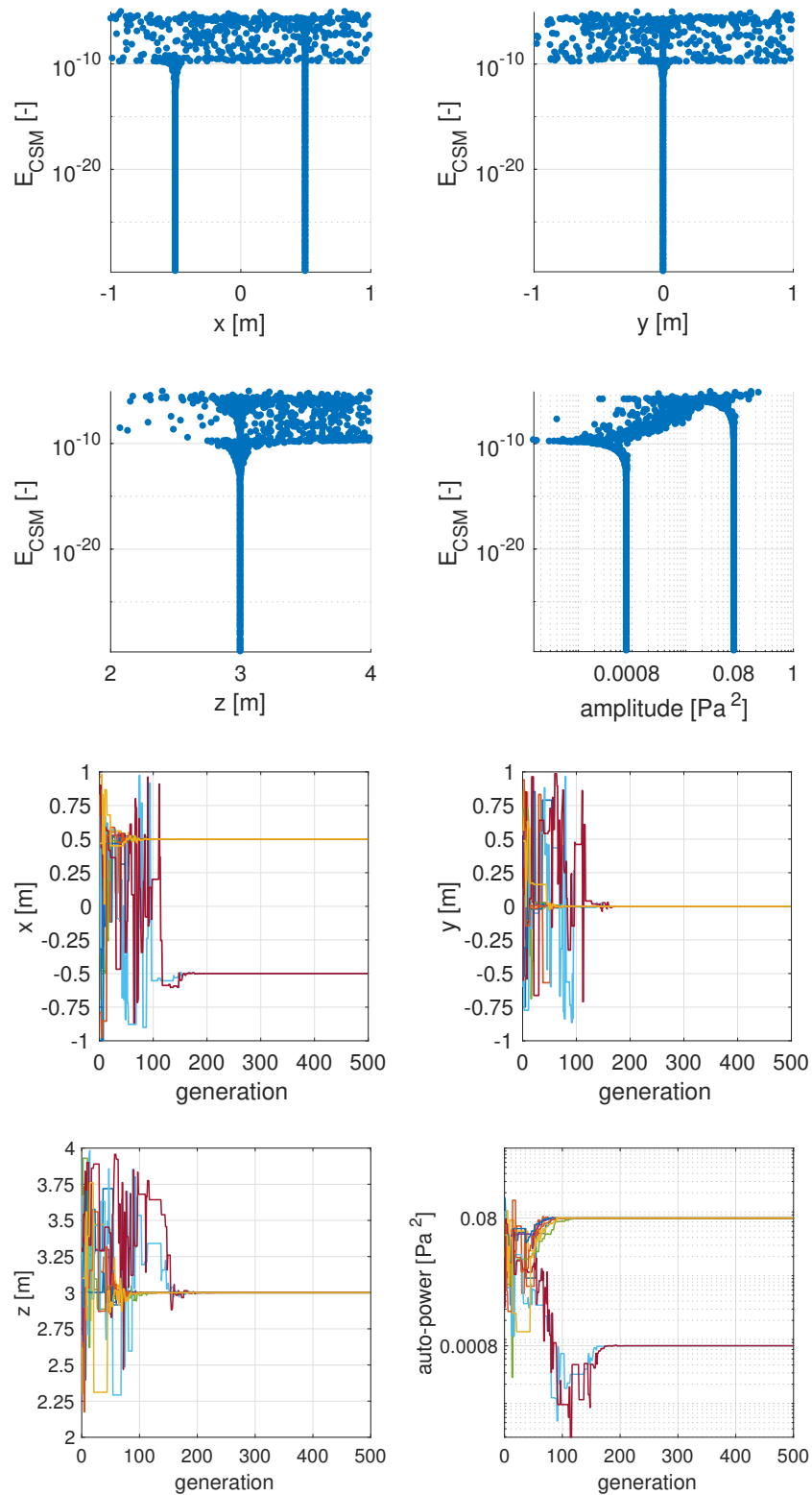


Figure 4.8: Energy landscape and convergence plots of GO with the CSM energy function, applied to two point sources placed at $(x,y,z) = (-0.5,0,3)$ with a SPL of 80 dB, and placed at $(x,y,z) = (0.5,0,3)$ with a SPL of 60 dB, both $f = 5000$ Hz. GO with the CSM energy is able to locate and quantify both sound sources correctly.

Results: distributed source simulations

This chapter presents the results of the distributed source simulations. Line source 1 is built from 100 point sources of 60 dB and $f = 2000$ Hz, with a spacing of 1 cm between the sources, see the left plot of Figure 3.3. Noise with five different SNRs is added, resulting in six data sets for line source 1: no noise, SNR = 5 dB, SNR = -2.5 dB, SNR = -10 dB, SNR = -15 dB and SNR = -20 dB. By making a time-averaged CSM, see Equation 2.8, noise has more effect on the auto-powers than on the cross-powers. Therefore, applying Diagonal Removal (DR), i.e. removing the diagonal of the CSM, may yield improved results. To test this, the results of the distributed source simulations are made for both with and without DR. The order of the presentation of the results will be: CB - DAMAS - SPI.

Applying CB without DR results in the six plots of Figure 5.2. For the data set without noise and the data set with SNR = 5 dB, the line source is clearly visible. From the data set with SNR = -2.5 dB and beyond, the effect of the noise is becoming more and more dominant. The result is that line source 1 becomes less visible with decreasing SNR. For point sources, CB is well able to determine the source locations as well as the auto-powers. For distributed sources, however, CB is well able to determine the source location, yet not the auto-power.

Applying CB with DR results in the five plots of Figure 5.3. CB with DR is not applied to the 'no noise' data set, since removing the diagonal from the CSM only has a positive effect when noise is present. In general, Figure 5.3 shows that DR resulted in a much smaller effect of the noise, compared to the CB plots without DR, see Figure 5.2. The CB plots with SNR = 5 dB - SNR = -10 dB are very similar to the CB plot without noise. For the plot with SNR = -15 dB the noise is more visible and for the plot with SNR = -20 dB one sees that the noise has really disturbed the signal.

Applying DAMAS without DR results in the six plots of Figure 5.4. Line source 1 is clearly visible in the DAMAS plots without noise and SNR = 5 dB. With decreasing SNR, the effect of the noise becomes more dominant in the plots. To check whether DAMAS gives the correct OSPL for line source 1, the source auto-powers in $[\text{Pa}^2]$ at grid points $x = -0.5$ to $x = +0.5$ and $y = 0$ are summed and converted to a SPL in [dB] via Equation 2.4. The expected OSPL for line source 1 is 80 dB, see Equation 2.5. For the six data sets of line source 1, the summed DAMAS results are given in Table 5.1. For the data set without noise, the summed DAMAS result is exactly equal to the expected value of 80 dB. For the data sets with SNR = 5 dB and SNR = -2.5 dB, the summed DAMAS results are close to the expected value. In general, the summed DAMAS results increase with decreasing SNR, because in addition to the signal, auto-powers due to the noise are summed.

Table 5.1: The summed DAMAS results for line source 1 without DR. These results are calculated by summing the source auto-powers of grid points $x = -0.5$ to $x = +0.5$ and $y = 0$ for the six data sets of Figure 5.4.

DAMAS <i>without</i> DR						
data set	no noise	SNR 5 dB	SNR -2.5 dB	SNR -10 dB	SNR -15 dB	SNR -20 dB
OSPL	80.00 dB	80.03 dB	80.35 dB	81.60 dB	84.10 dB	87.98 dB

Applying DAMAS with DR results in the five plots of Figure 5.5. Similar to CB, for all plots the effect of the noise is less dominant compared to the DAMAS plots without DR. Again, to check whether DAMAS gives

the correct OSPL for line source 1, the source auto-powers in $[\text{Pa}^2]$ at grid points $x = -0.5$ to $x = +0.5$ and $y = 0$ are summed and converted to a SPL in $[\text{dB}]$ via Equation 2.4. The summed DAMAS results with DR are given in Table 5.2. As one can see, the summed DAMAS results for line source 1 with DR are close to the expected result of 80 dB. For all data sets, the calculated OSPL is approximately 0.6 dB below the expected value.

Table 5.2: The summed DAMAS results for line source 1 with DR. These results are calculated by summing the source auto-powers of grid points $x = -0.5$ to $x = +0.5$ and $y = 0$ for the six data sets of Figure 5.5.

DAMAS <i>with</i> DR					
data set	SNR 5 dB	SNR -2.5 dB	SNR -10 dB	SNR -15 dB	SNR -20 dB
OSPL	79.42 dB	79.43 dB	79.41 dB	79.48 dB	79.33 dB

SPI point without DR is applied to line source 1 with three different integration grids. Grid 5.1 is defined on top of the point sources of line source 1, thus -0.5 to $+0.5$ with steps of 1 cm for the x-coordinates and $y = 0$. Grid 5.2 is larger in the y-direction compared to grid 1, thus -0.5 to $+0.5$ with steps of 1 cm for the x-coordinates and -0.25 to $+0.25$ with steps of 1 cm for the y-coordinates. Grid 5.3 is larger in both the x- and y-direction compared to grid 1, thus -0.75 to $+0.75$ with steps of 1 cm for the x-coordinates and -0.25 to $+0.25$ with steps of 1 cm for the y-coordinates. For a visualization of the integration grids, see Figure 5.1. When applying SPI point, the expected result is the OSPL of line source 1, i.e. 80 dB. The results of SPI point without DR for grids 5.1, 5.2 and 5.3 are given in Table 5.3.

Table 5.3: SPI point without DR applied to line source 1 for three different integration grids. For a visualization of the integration grids, see Figure 5.1.

SPI point <i>without</i> DR						
data set	no noise	SNR 5 dB	SNR -2.5 dB	SNR -10 dB	SNR -15 dB	SNR -20 dB
OSPL, grid 5.1	79.66 dB	79.76 dB	80.18 dB	81.98 dB	84.78 dB	88.75 dB
OSPL, grid 5.2	79.69 dB	79.87 dB	80.61 dB	83.32 dB	86.82 dB	91.19 dB
OSPL, grid 5.3	80.04 dB	80.27 dB	81.24 dB	84.50 dB	88.29 dB	92.82 dB

Applying SPI point with DR yields the results of Table 5.4. Integration grids 5.1, 5.2 and 5.3 are the same as for SPI point without DR, see Figure 5.1. Again, the expected result when applying SPI point is the OSPL of line source 1, i.e. 80 dB.

Table 5.4: SPI point with DR applied to line source 1 for three different integration grids. For a visualization of the integration grids, see Figure 5.1.

SPI point <i>with</i> DR					
data set	SNR 5 dB	SNR -2.5 dB	SNR -10 dB	SNR -15 dB	SNR -20 dB
OSPL, grid 5.1	79.30 dB	79.30 dB	79.29 dB	79.35 dB	79.32 dB
OSPL, grid 5.2	79.01 dB	79.01 dB	78.99 dB	79.10 dB	78.98 dB
OSPL, grid 5.3	79.30 dB	79.31 dB	79.29 dB	79.39 dB	79.37 dB

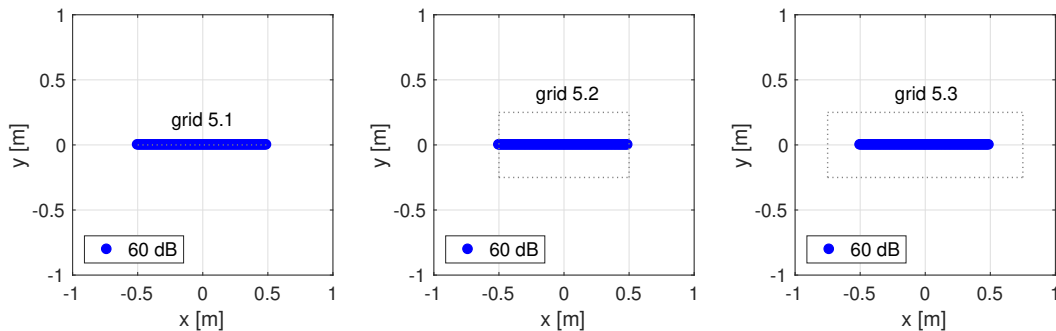


Figure 5.1: Three integration grids for line source 1: 100 point sources of 60 dB and $f = 2000$ Hz, with a spacing of 1 cm between the sources. Left: grid 5.1. Center: grid 5.2. Right: grid 5.3.

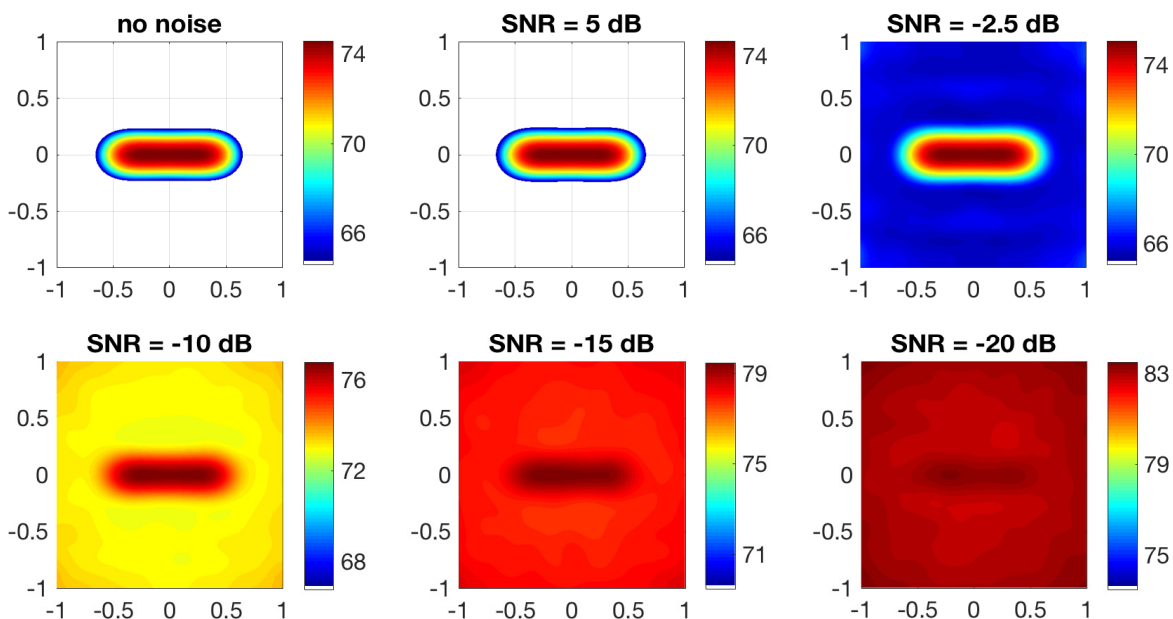


Figure 5.2: CB without DR applied to line source 1, i.e. 100 point sources of 60 dB and $f = 2000$ Hz, with a spacing of 1 cm between the sources. Noise with five different SNRs is added, resulting in six CB plots. For the data set without noise and the data set with SNR = 5 dB, the line source is clearly visible. From the data set with SNR = -2.5 dB and beyond, the noise is becoming more and more dominant. The result is that line source 1 becomes less visible with decreasing SNR.

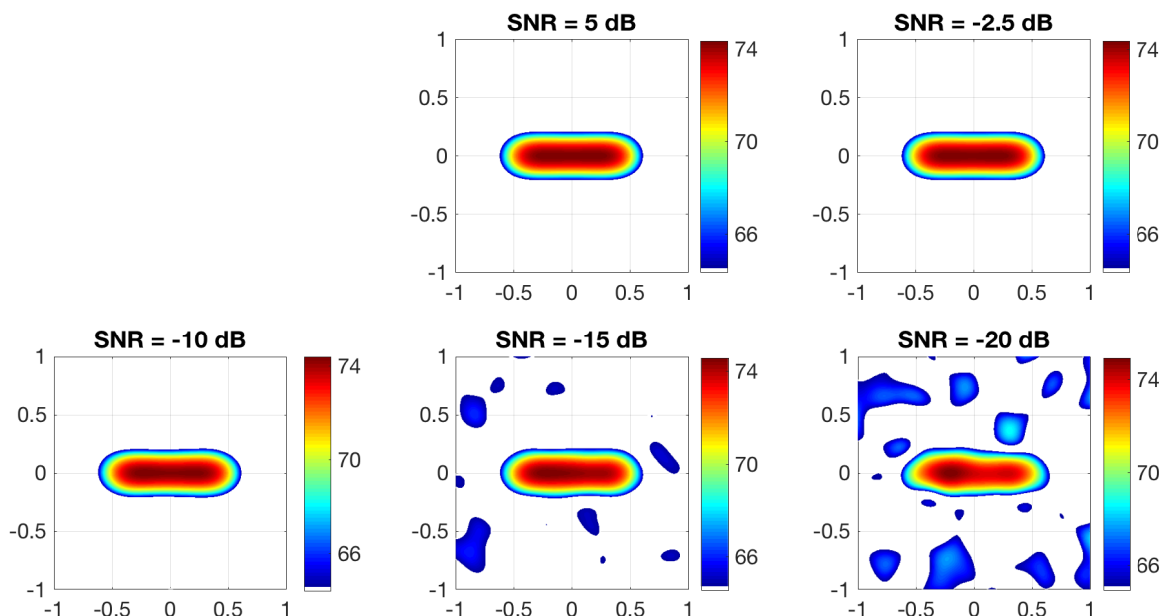


Figure 5.3: CB with DR applied to line source 1, i.e. 100 point sources of 60 dB and $f = 2000$ Hz, with a spacing of 1 cm between the sources. Noise with five different SNRs is added and diagonal removal is applied. The plots with SNR = 5 dB - SNR = -10 dB are very similar to the plot without noise. For the plot with SNR = -15 dB the noise is more visible and for the plot with SNR = -20 dB one sees that the noise has really disturbed the signal.

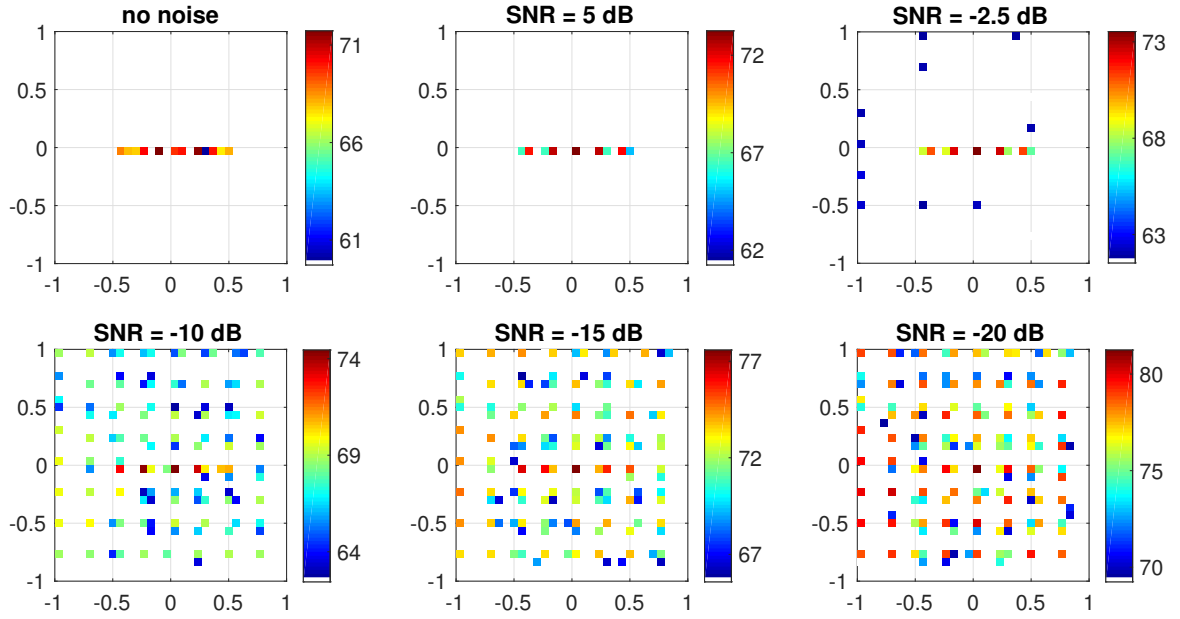


Figure 5.4: DAMAS without DR applied to line source 1, i.e. 100 point sources of 60 dB and $f = 2000$ Hz, with a spacing of 1 cm between the sources. Noise with five different SNRs is added, resulting in six DAMAS plots. Line source 1 is clearly visible in the DAMAS plots without noise and SNR = 5 dB. With decreasing SNR, the effect of the noise becomes more dominant in the plots.

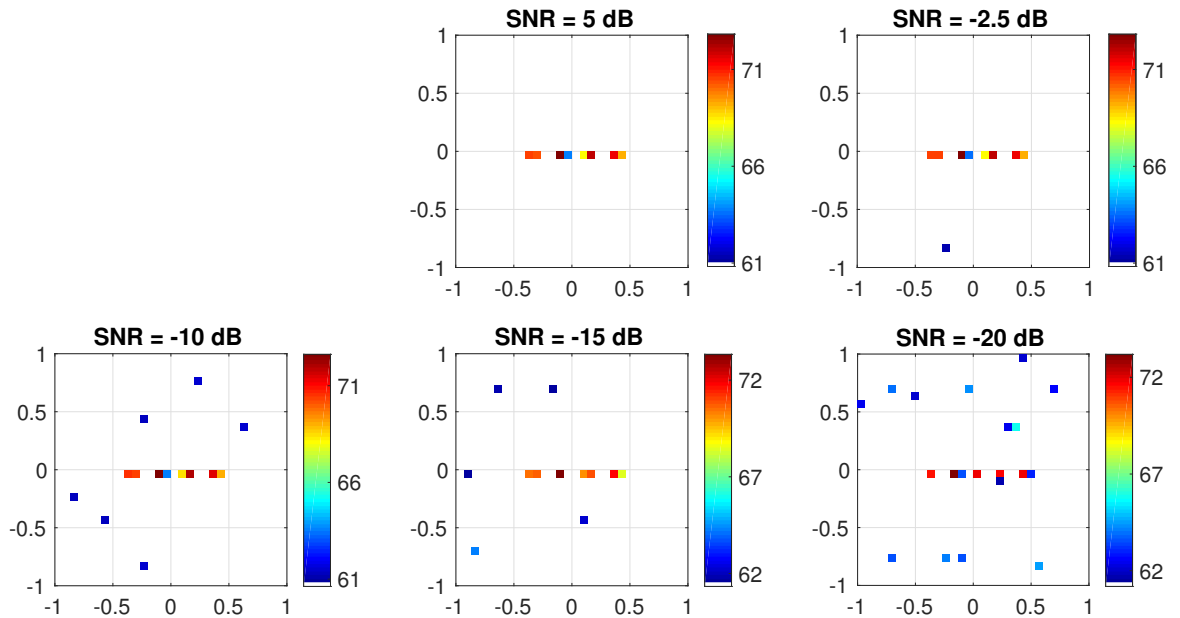


Figure 5.5: DAMAS with DR applied to line source 1, i.e. 100 point sources of 60 dB and $f = 2000$ Hz, with a spacing of 1 cm between the sources. Noise with five different SNRs is added and diagonal removal is applied. For all plots, the effect of the noise is less visible compared to the DAMAS plots without diagonal removal.

Line source 2 is a line source built from 99 point sources of $f = 2000$ Hz, divided in three parts of 33 sources, see the right plot of Figure 3.3. In the first part the point sources have a SPL of 60 dB, in the second part 55 dB and in the third part 65 dB. Noise with five different SNRs is added, resulting in six data sets for line source 2: no noise, SNR = 5 dB, SNR = -2.5 dB, SNR = -10 dB, SNR = -15 dB and SNR = -20 dB.

Applying CB without DR results in the six plots of Figure 5.7. Because one already saw the results of CB without DR for line source 1, the results for line source 2 are in line with expectations. For the data set without noise and the data set with SNR = 5 dB, line source 2 is clearly visible. From the data set with SNR = -2.5 dB and beyond, the noise is becoming more and more dominant. The result is that line source 2 becomes less visible with decreasing SNR.

Applying CB with DR results in the five plots of Figure 5.8. Removing the diagonal from the CSM has removed a large effect of the noise. The CB plots with SNR = 5 dB - SNR = -10 dB are very similar to the CB plot without noise. For the plot with SNR = -15 dB the noise is more visible and for the plot with SNR = -20 dB one sees that the noise has really disturbed the signal.

Applying DAMAS without DR results in the six plots of Figure 5.9. Line source 2 is clearly visible in the DAMAS plots without noise, with SNR = 5 dB and with SNR = -2.5 dB. With decreasing SNR, the effect of the noise becomes more dominant in the plots. To check whether DAMAS gives the correct OSPL for line source 2, the source auto-powers in $[\text{Pa}^2]$ at grid points $x = -0.5$ to $x = +0.5$ and $y = 0$ zero are summed and converted to a SPL in [dB] via Equation 2.4. The expected OSPL for line source 2 is 81.70 dB, see Equation 2.5. For the six data sets of line source 2, the summed DAMAS results are given in Table 5.5. For the data set without noise, with SNR = 5 dB and SNR = -2.5 dB, the summed DAMAS results correspond well with the expected outcome of 81.70 dB. In general, the summed DAMAS results degrade with decreasing SNR.

Table 5.5: The summed DAMAS results for line source 2 without DR. These results are calculated by summing the source auto-powers of grid points $x = -0.5$ to $x = +0.5$ and $y = 0$ for the six data sets of Figure 5.9.

DAMAS <i>without</i> DR						
data set	no noise	SNR 5 dB	SNR -2.5 dB	SNR -10 dB	SNR -15 dB	SNR -20 dB
OSPL	81.70 dB	81.75 dB	82.06 dB	83.44 dB	85.91 dB	89.57 dB

Applying DAMAS with DR results in the five plots of Figure 5.10. For all plots, the effect of the noise is less visible compared to the DAMAS plots without DR. Again, to check whether DAMAS gives the correct OSPL for line source 2, the summed DAMAS results with DR are given in Table 5.6. As one can see, the summed DAMAS results for line source 2 with DR are close to the expected result of 81.70 dB. For all data sets, the calculated OSPL is approximately 0.6 dB below the expected value.

Table 5.6: The summed DAMAS results for line source 2 with DR. These results are calculated by summing the source auto-powers of grid points $x = -0.5$ to $x = +0.5$ and $y = 0$ for the six data sets of Figure 5.10.

DAMAS <i>with</i> DR					
data set	SNR 5 dB	SNR -2.5 dB	SNR -10 dB	SNR -15 dB	SNR -20 dB
OSPL	81.12 dB	81.12 dB	81.11 dB	81.14 dB	81.03 dB

SPI point without DR is applied to line source 2 with the same integration grids used for line source 1, see Figure 5.1. When applying SPI point, the expected result is the OSPL of line source 2, i.e. 81.70 dB. The results of SPI point for grids 5.1, 5.2 and 5.3 are given in Table 5.10.

Table 5.7: SPI point without DR applied to line source 2 for three different integration grids. For a visualization of the integration grids, see Figure 5.1.

SPI point <i>without</i> DR						
data set	no noise	SNR 5 dB	SNR -2.5 dB	SNR -10 dB	SNR -15 dB	SNR -20 dB
OSPL, grid 5.1	81.24 dB	81.34 dB	81.77 dB	83.60 dB	86.44 dB	90.42 dB
OSPL, grid 5.2	81.28 dB	81.46 dB	82.22 dB	84.96 dB	88.49 dB	92.88 dB
OSPL, grid 5.3	81.71 dB	81.99 dB	82.95 dB	86.19 dB	89.99 dB	94.50 dB

Applying SPI point with DR yields the results of Table 5.8. Again, the expected result when applying SPI point is the OSPL of line source 2, i.e. 81.70 dB.

Table 5.8: SPI point with DR applied to line source 2 for three different integration grids. For a visualization of the integration grids, see Figure 5.1.

SPI point <i>with</i> DR					
data set	SNR 5 dB	SNR -2.5 dB	SNR -10 dB	SNR -15 dB	SNR -20 dB
OSPL, grid 5.1	80.87 dB	80.87 dB	80.85 dB	80.88 dB	80.99 dB
OSPL, grid 5.2	80.62 dB	80.62 dB	80.59 dB	80.62 dB	81.96 dB
OSPL, grid 5.3	81.06 dB	81.07 dB	81.04 dB	81.07 dB	81.46 dB

Inverse SPI without DR is applied to line source 2. Integration grid 5.4 has points $x = -0.49$ to $x = -0.17$ and $y = -0.25$ to $y = +0.25$, integration grid 5.5 has points $x = -0.16$ to $x = +0.16$ and $y = -0.25$ to $y = +0.25$, and integration grid 5.6 has points $x = +0.17$ to $x = +0.49$ and $y = -0.25$ to $y = +0.25$. For integration grids 5.4, 5.5 and 5.6, inverse SPI is applied simultaneously. For a visualization of integration grids 5.4, 5.5 and 5.6, see the left plot of Figure 5.6. For the six data sets of line source 2, the results are found in Table 5.9.

Table 5.9: Inverse SPI without DR applied with integration grids 5.4, 5.5 and 5.6 of line source 2. For a visualization of the integration grids, see the left plot of Figure 5.6.

inverse SPI <i>without</i> DR							
data set	expec.	no noise	SNR 5 dB	SNR -2.5 dB	SNR -10 dB	SNR -15 dB	SNR -20 dB
OSPL, grid 5.4	75.19 dB	75.15 dB	75.29 dB	75.95 dB	78.40 dB	81.77 dB	86.09 dB
OSPL, grid 5.5	70.19 dB	70.15 dB	70.52 dB	71.94 dB	75.93 dB	80.04 dB	84.72 dB
OSPL, grid 5.6	80.19 dB	80.15 dB	80.20 dB	80.41 dB	81.47 dB	83.47 dB	86.77 dB

SPI point without DR is applied to line source 2 with integration grids 5.4, 5.5 and 5.6 in order to compare the performances of inverse SPI and SPI point. The SPI point results are found in Table 5.10. Comparing Tables 5.9 and 5.10 shows that inverse SPI is perfectly able to determine the source auto-powers of the three parts of line source 2, where SPI point overestimates the source auto-powers of the middle part, i.e. the 55 dB part. When one has a distributed source built from point sources with varying source auto-powers, inverse SPI is the preferred algorithm.

Table 5.10: SPI point without DR applied with integration grids 5.4, 5.5 and 5.6 of line source 2.

SPI point <i>without</i> DR							
data set	expec.	no noise	SNR 5 dB	SNR -2.5 dB	SNR -10 dB	SNR -15 dB	SNR -20 dB
OSPL, grid 5.4	75.19 dB	74.78 dB	74.94 dB	75.64 dB	78.20 dB	81.63 dB	85.99 dB
OSPL, grid 5.5	70.19 dB	74.79 dB	74.95 dB	75.64 dB	78.21 dB	81.59 dB	85.92 dB
OSPL, grid 5.6	80.19 dB	79.55 dB	79.61 dB	79.85 dB	81.02 dB	83.16 dB	86.58 dB

To test the effect of employing more integration grids for inverse SPI, nine instead of three integration grids are defined. The nine integration grids are labelled grid 5.7 - 5.15, see the center plot of Figure 5.6. To keep a clear overview of the results, only the 'no noise' data set results are presented in Table 5.11.

Table 5.11: Inverse SPI without DR applied with nine integration grids to line source 2. For a visualization of the integration grids, see the center plot of Figure 5.6.

inverse SPI nine integration grids		
data set	expec.	no noise
OSPL, grid 5.7	70.41 dB	70.41 dB
OSPL, grid 5.8	70.41 dB	70.41 dB
OSPL, grid 5.9	70.41 dB	70.41 dB
OSPL, grid 5.10	65.41 dB	65.41 dB
OSPL, grid 5.11	65.41 dB	65.41 dB
OSPL, grid 5.12	65.41 dB	65.41 dB
OSPL, grid 5.13	75.41 dB	75.41 dB
OSPL, grid 5.14	75.41 dB	75.41 dB
OSPL, grid 5.15	75.41 dB	75.41 dB

For simulations, the source locations are known to the researcher. Placing the integration grids for SPI is therefore easy, i.e. the integration grids for line source 2 enclose the three parts of line source 2 perfectly. For experimental data, however, the source locations are not known in advance. This makes it difficult to define the integration grids. Therefore, it has been tested what the effect is on the inverse SPI results if the integration grids are not perfectly placed. Inverse SPI without diagonal removal is applied to line source 2, with integration grids 5.16, 5.17 and 5.18. These three integration grids have been shifted 10 cm to the left with respect to grids 5.4, 5.5 and 5.6, see the right plot of Figure 5.6. Grid 5.16 encloses 23 sources of 60 dB, thus the expected SPI result is 73.62 dB, see Equation 2.5. Grid 5.17 encloses 23 sources of 55 dB and 10 sources of 60 dB, thus the expected SPI result is 72.37 dB and grid 5.18 encloses 23 sources of 65 dB and 10 sources of 55 dB, thus the expected SPI result is 78.80 dB. The inverse SPI results are shown in Table 5.12. For grids 5.16 and 5.18, the results correspond to the expected outcomes with a margin of 0.8 dB. However, for grid 5.17 the result deviates more than 4 dB from the expected result.

This test shows that there is a big advantage in accurately placing the integration grids. When it is unclear where the sources are located, it is better to adopt smaller integration grids, as in the case of nine integration grids in Table 5.11. Inaccuracies result from using less and larger integration grids.

Table 5.12: Inverse SPI without DR applied with three shifted integration grids to line source 2. For a visualization of the integration grids, see the right plot of Figure 5.6.

inverse SPI shifted integration grids		
data set	expec.	no noise
OSPL, grid 5.16	73.62 dB	74.41 dB
OSPL, grid 5.17	72.37 dB	68.15 dB
OSPL, grid 5.18	78.80 dB	79.68 dB

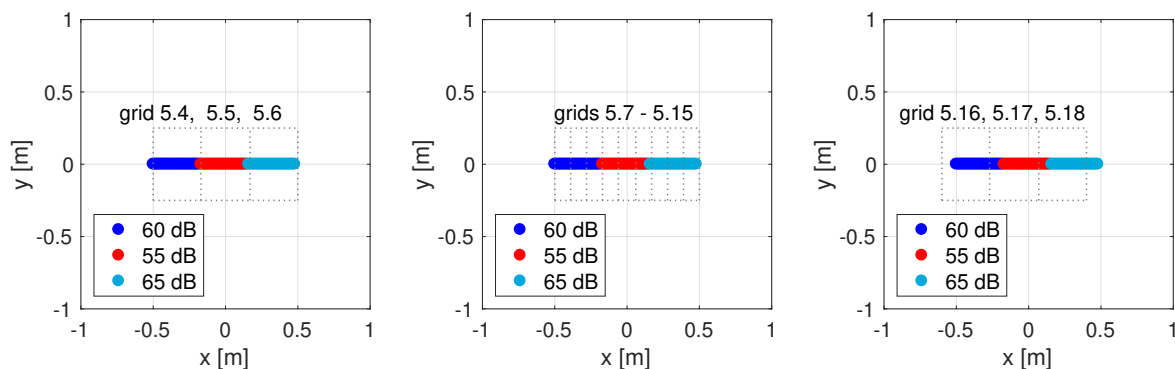


Figure 5.6: Integration grids for line source 2: 99 point sources of $f = 2000$ Hz, divided in three parts of 33 sources. In the first part the point sources have a SPL of 60 dB, in the second part 55 dB and in the third part 65 dB. Left: from left to right, grid 5.4, grid 5.5 and grid 5.6. Center: from left to right, grid 5.7, grid 5.8, grid 5.9, grid 5.10, grid 5.11, grid 5.12, grid 5.13, grid 5.14, grid 5.15. Right: from left to right, grid 5.16, grid 5.17, grid 5.18.

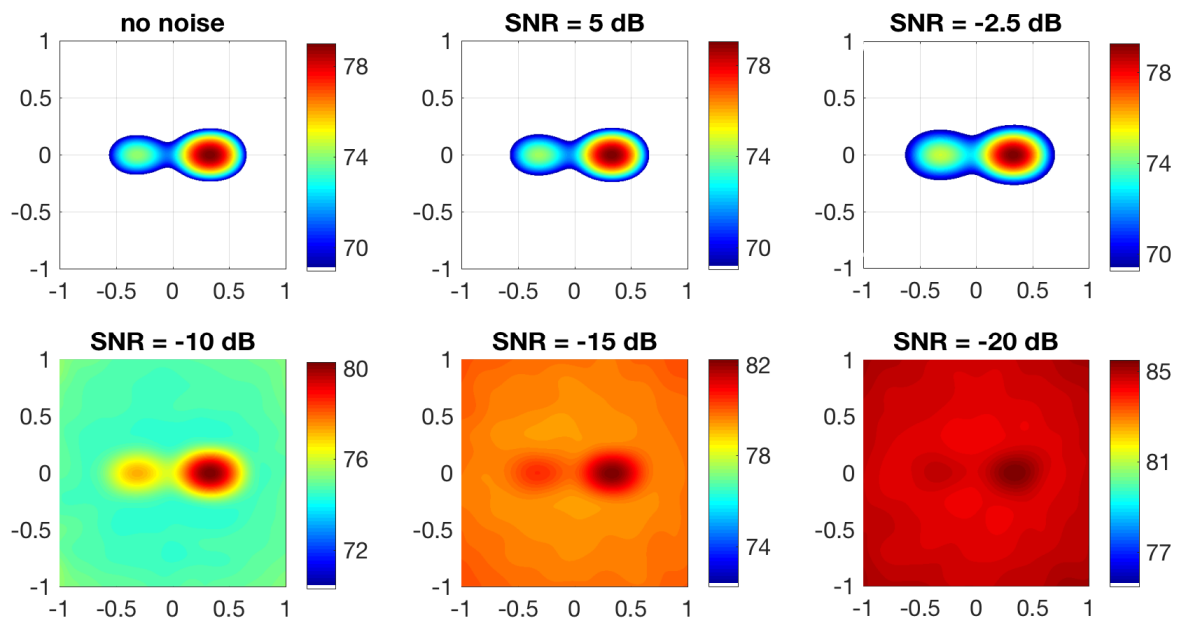


Figure 5.7: CB without DR applied to line source 2, i.e. 99 point sources of $f = 2000$ Hz, divided in three parts with different SPLs. Noise with five different SNRs is added, resulting in six CB plots. For the data set without noise and the data set with SNR = 5 dB, the line source is clearly visible. From the data set with SNR = -2.5 dB and beyond, the noise is becoming more and more dominant. The result is that line source 1 becomes less visible with decreasing SNR.

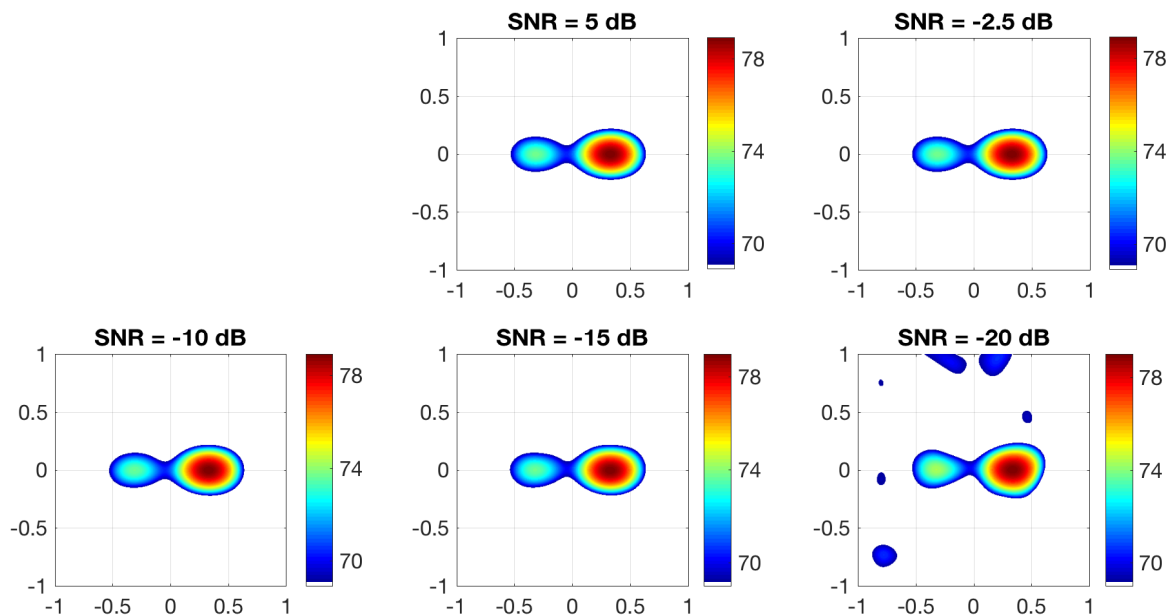


Figure 5.8: CB with DR applied to line source 2, i.e. 99 point sources of $f = 2000$ Hz, divided in three parts with different SPLs. Noise with five different SNRs is added, resulting in six CB plots. The plots with SNR = 5 dB - SNR = -10 dB are very similar to the plot without noise. For the plot with SNR = -15 dB the noise is more visible and for the plot with SNR = -20 dB one sees that the noise has really disturbed the signal.

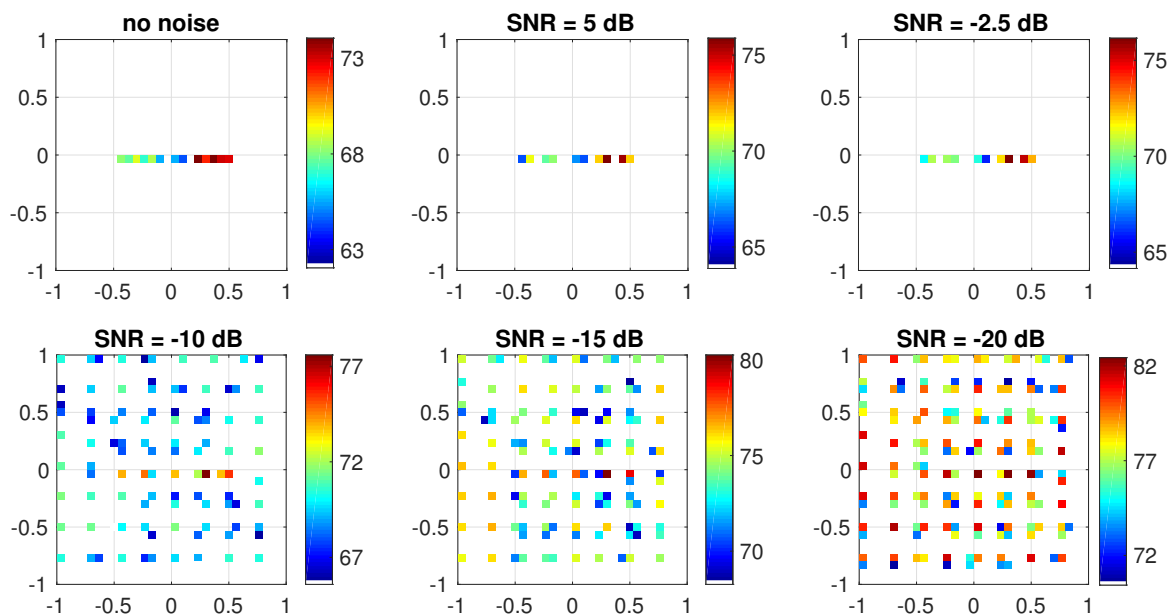


Figure 5.9: DAMAS without DR applied to line source 2, i.e. 99 point sources of $f = 2000$ Hz, divided in three parts with different SPLs. Noise with five different SNRs is added, resulting in six DAMAS plots. Line source 2 is clearly visible in the DAMAS plots without noise, SNR = 5 dB and SNR = -2.5 dB. With decreasing SNR, the effect of the noise becomes more dominant in the plots.

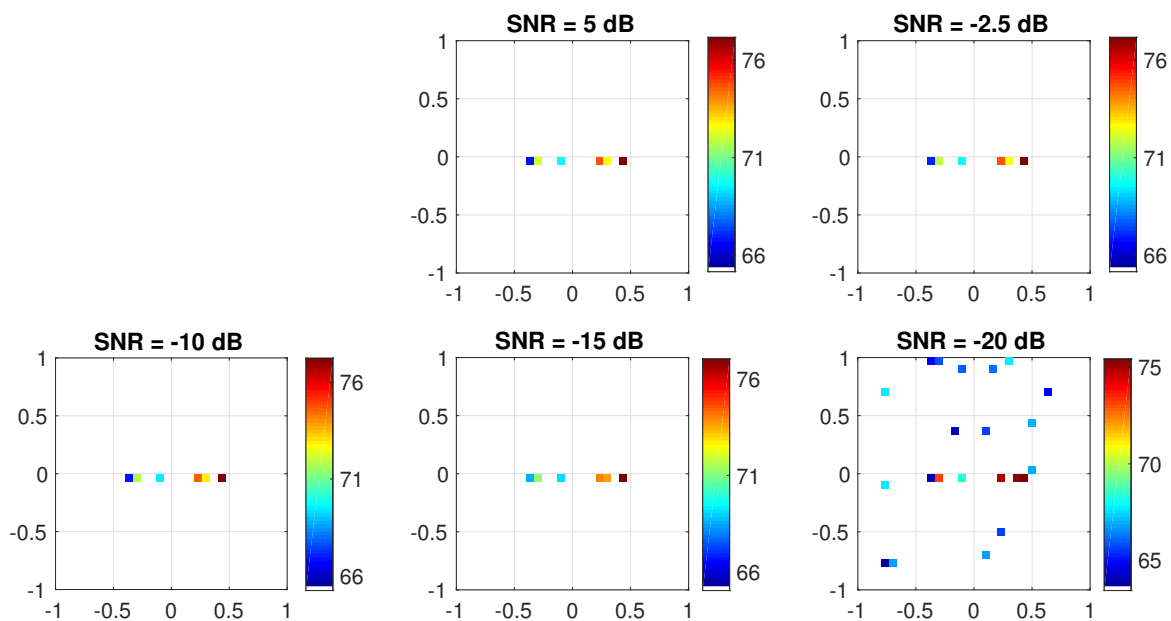


Figure 5.10: DAMAS with DR applied to line source 2, 99 point sources of $f = 2000$ Hz, divided in three parts with different SPLs. Noise with five different SNRs is added, resulting in six DAMAS plots. For all plots, the effect of the noise is less visible compared to the DAMAS plots without diagonal removal.

6

Investigating the performance of GO in identifying closely spaced sound sources

In this chapter it is investigated whether GO with the CSM energy function is able to accurately identify two point sources placed at a distance below the Rayleigh limit from each other. This research encompasses placing two point sources closer and closer together, to inspect up to what distance GO can identify the sources as two separate sources. First, the research is carried out for simulations, to see what GO with the CSM energy function is theoretically capable of. Then the research is carried out for experimental data, to have the performance of GO tested in practice.

For simulations, two cases are studied. In case 1 the two point sources have the same SPL, 80 dB, and the same frequency, $f = 1000$ Hz. The distance between the source plane and microphone array is 3 m. The aperture of the microphone array is 2 m. With the speed of sound of 343 m/s, the Rayleigh limit is 0.63 m, see Equation 2.14. The two point sources are first placed 90 cm apart and are placed closer together in steps of 5 cm. Three data sets are used in case 1, the first without noise, the second with SNR = -2.5 dB and the third with SNR = -20 dB. To inspect whether removing the diagonal from the CSM affects the correct identification of the two sources, the data sets with noise are employed two times: with and without diagonal removal. Case 2 is identical to case 1 in all aspects, except that the two sources now have SPLs 80 dB and 70 dB, respectively.

To compare the performance of GO to CB, CB is applied to case 1 (two point sources of 80 dB). The results are shown in Figure 6.2. When the distance between the two sources is 90 cm, CB clearly shows two separate sources. In steps of 5 cm, the sources become more difficult to distinguish. At and below the Rayleigh limit, one can no longer say with certainty whether one or two sources are present.

Now it is time to look at the performance of GO. GO with the CSM energy function is applied to cases 1 and 2. The algorithm searches for eight parameters: the (x,y,z) -coordinates and source auto-power of the left source and the (x,y,z) -coordinates and source auto-power of the right source. In order to keep the results of this research clear, only the x-coordinates are shown in the results. The algorithm settings are: $p_C = 0.75$, $F = 0.40$, $N_{\text{runs}} = 3$, $q = 128$ and $N_G = 600$. Out of the three runs, the solution set with the lowest energy function value is plotted. Figure 6.3 shows eight plots. The four plots on the left belong to case 1, i.e. two sources of 80 dB and the four plots on the right belong to case 2, i.e. two sources of 80 dB and 70 dB, respectively. In the top six plots, the x-coordinates of the two sources are plotted against the distance between the sources. In the bottom two plots, the CSM energy function values of the solution sets are plotted against the distance between the sources.

With simulations, five things are learned from the investigation of the performance of GO in identifying closely spaced sound sources:

1. For the cases without noise the two sources are found with ease, spaced up to 5 cm apart. In this aspect, GO offers a considerable improvement compared to CB. At 5 cm distance there is no 'perfect match' between the measured and modeled CSM, but a good enough match to find the sources with a margin of error of 2 cm. With an increasing number of generations N_G , this margin of error decreases.

2. With increasing noise, GO is less able to accurately identify the sound sources.
3. Removing the diagonal of the CSM ensures a better match between the measured and modeled CSM compared to not removing the diagonal of the CSM.
4. Adding noise has a greater effect on the weaker source (70 dB) compared to the effect on the stronger source (80 dB). In other words, the stronger source is relatively better identified than the weaker source, when noise is present. This is logical to understand because the OSPL of the signal is used in the expressions of the SNR.
5. In the absence of noise, the CSM energy function values decrease as the distance between the two sources increases. With noise, by contrast, the CSM energy function values remain approximately constant with varying distance between the sources. An explanation for this is that in the absence of noise, a perfect match between the measured and modeled CSM is possible and that the perfect match is more easily found with a greater distance between the sources. Adding noise distorts the matching between modeled and measured CSM in such a way, that the distance between the sources no longer affects the CSM energy function values.

At the beginning of this chapter it was already stated that this research is carried out with experimental data as well, to have the performance of GO tested in practice. The two experimental data sets employed in this research are the sets with two small speakers broadcasting white noise, placed 80 and 25 cm apart, respectively, see the left plots of Figures 3.4 and 3.5. The two sources are now at a fixed distance from each other, which is why this research is conducted with varying frequencies. For frequencies of $f = 100 - 5000$ Hz in steps of 100 Hz, GO is applied to the two experimental data sets. The algorithm settings are the same as for the simulations: $p_C = 0.75$, $F = 0.40$, $N_{\text{runs}} = 3$, $q = 128$ and $N_G = 600$. The sound speed is again $c = 343$ m/s, the array aperture is 1 m and the distance between the source plane and the array plane is 1.87 m. For the data set where the sources are placed 80 cm apart the frequency corresponding to the Rayleigh limit is 978 Hz. For the data set where the sources are 25 cm apart the frequency corresponding to the Rayleigh limit is 3130 Hz. The results can be seen in Figure 6.1.

From the investigation of the performance of GO in identifying closely spaced sound sources with experimental data, one learns that for frequencies of 600 Hz and onwards, the two sources are correctly identified by GO with a margin of error of 2 cm for both experimental data sets (two sources placed 25 and 80 cm apart). DR does not significantly improve the experimental results. Because the experimental data sets are recorded in an anechoic room and subsequently a time-averaged CSM is constructed, there are hardly any distortions in the signal and DR does not provide a large improvement.

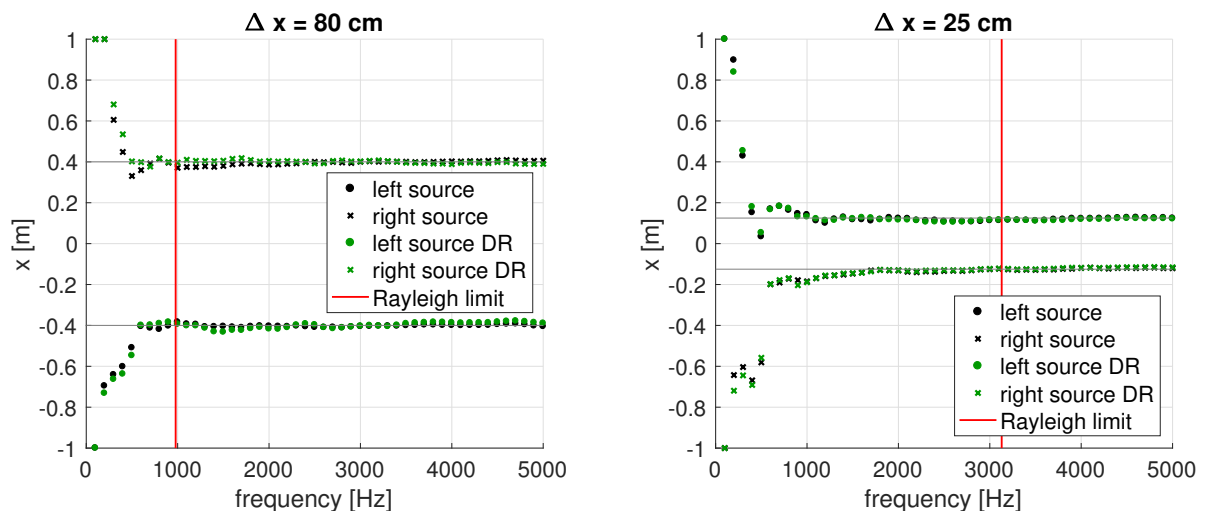


Figure 6.1: GO applied to the experimental data sets with two small speakers broadcasting white noise, placed 80 and 25 cm apart, respectively. Left: For the two sources 80 cm apart the frequency corresponding to the Rayleigh limit is $f = 978$ Hz. Right: For the two sources 25 cm apart the frequency corresponding to the Rayleigh limit is $f = 3130$ Hz.

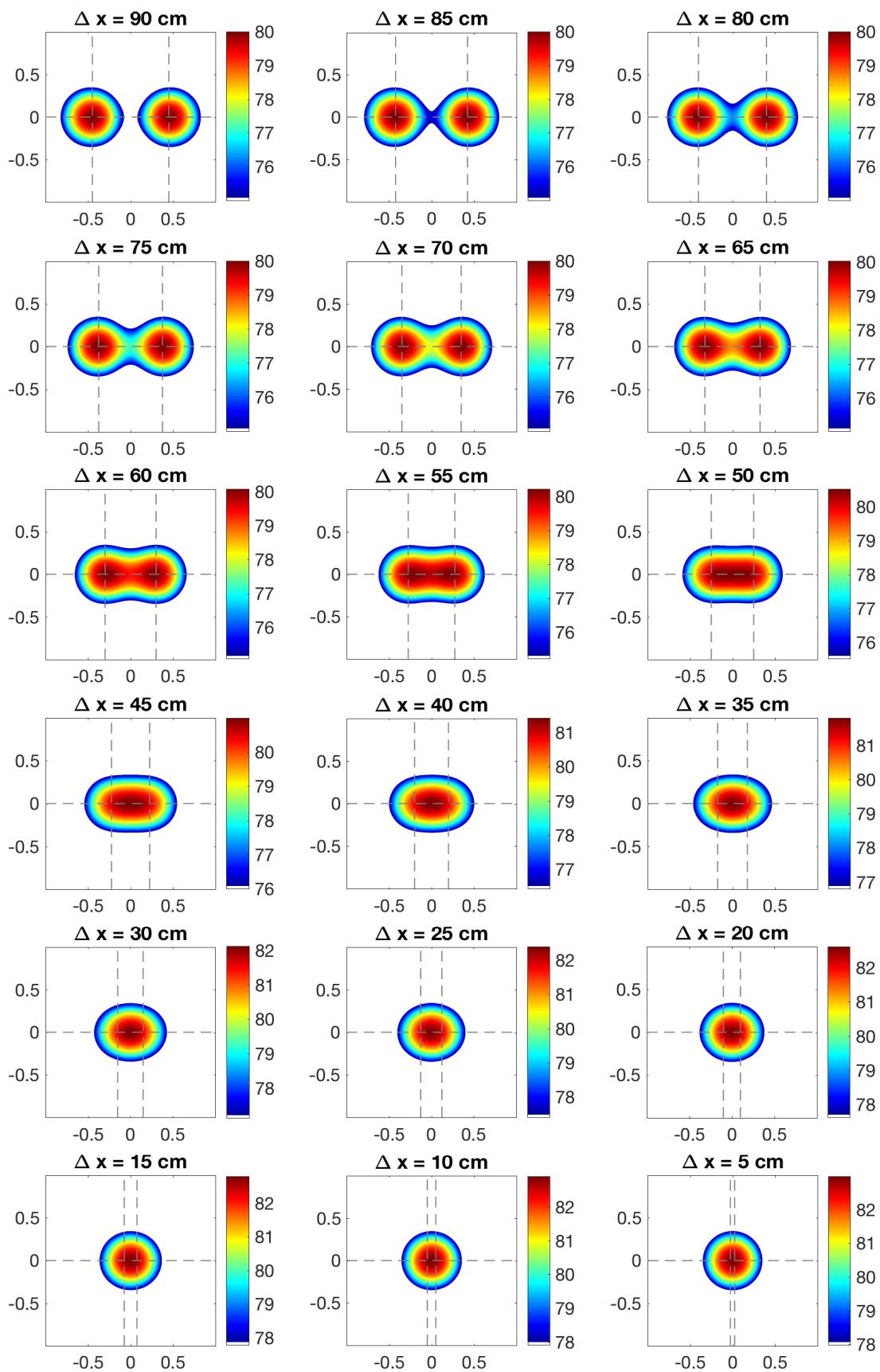


Figure 6.2: CB applied to case 1 of the Rayleigh research: two sources of 80 dB placed closer together in steps of 5 cm. The Rayleigh limit is 0.63 m.

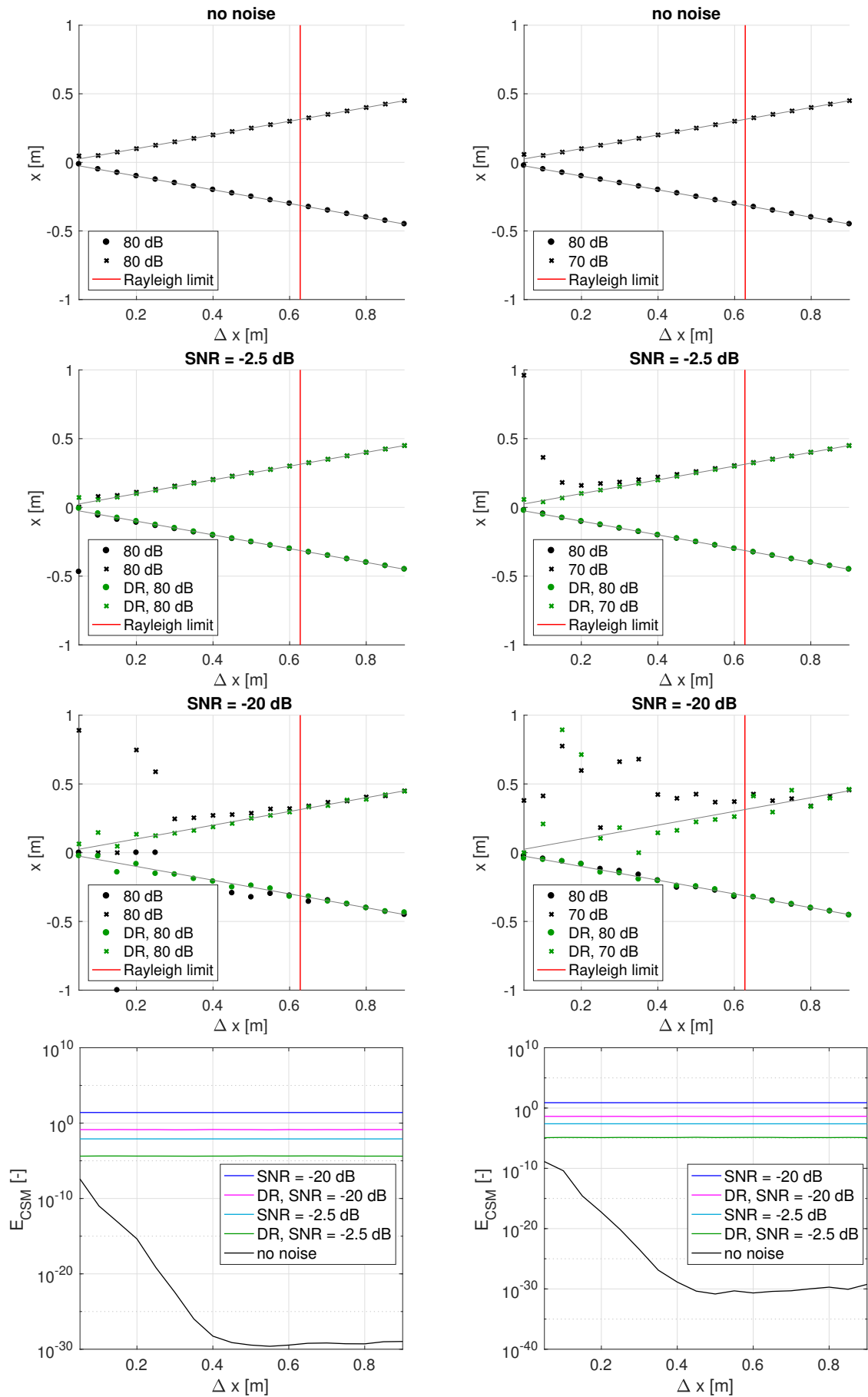


Figure 6.3: GO applied to cases 1 and 2 of the Rayleigh research. The four plots on the left belong to case 1, i.e. two sources of 80 dB and the four plots on the right belong to case 2, i.e. two sources of 80 dB and 70 dB, respectively.

The two new acoustic imaging techniques applied to experimental data

The six experimental data sets considered in this research consist of two speakers broadcasting white noise, placed 80 cm apart (both, left source, right source) and 25 cm apart (both, left source, right source). All four algorithms, i.e. CB, DAMAS, GO and SPI, are applied to these six experimental data sets.

To reduce the effect of side lobes for CB and DAMAS, the results are summed over 1/3 octave bands. For the frequency bands with center frequencies 315 Hz - 16000 Hz, the results are given in Figures 7.1 and 7.2 for CB and in Figures 7.3 and 7.4 for DAMAS.

For GO summing the results over 1/3 octave bands has no use. Because it is an optimization technique, it has no sidelobes. Therefore the results of the estimated parameters are plotted against frequency. Doing so, eight plots per dataset are acquired, i.e. two plots for the x-coordinates (left and right source), two plots for the y-coordinates (left and right source), two plots for the z-coordinates (left and right source) and two plots for the SPLs (left and right source). The GO results for the two speaker sources placed 80 cm apart are found in Figure 7.5 and placed 25 cm apart are found in Figure 7.6. In accordance with the results of Chapter 6, the source locations and auto-powers are accurately found for frequencies upward of approximately 1000 Hz. Chapter 4 showed that the CSM energy function outperforms the Bartlett processor in correctly identifying multiple sound sources. This is confirmed by Figures 7.5 and 7.6, especially at low frequencies the effect is clearly visible. Out of the (x,y,z)-coordinates, GO has the most difficulty in identifying the z-coordinate correctly. An explanation is that the z-coordinate has a smaller effect on the energy function value compared to the x- and y-coordinates, because the microphone array and source plane are aligned in the z-direction. An idea to correctly identify the (x,y,z)-coordinates with GO is to record the sound sources twice with the microphone array, rotating the array 90 degrees with respect to the sound sources at the second recording.

To compare the performance of CB, DAMAS, GO and SPI in correctly determining source auto-powers, the SPLs in [dB] of the left and right source of the 80 cm and 25 cm data sets are plotted against frequency in [Hz]. For all algorithms grids of 10x10 cm are used, centered around the left and right source and with a spacing of 1 cm between the grid points. For CB, the maximum auto-power in [Pa^2] is selected and converted to a SPL in [dB]. For DAMAS, the auto-powers in [Pa^2] are summed and subsequently converted to a SPL in [dB]. In order to know which algorithm performs best, the baseline is extracted from the one-source data sets, i.e. the left or right source switched on only as shown in the center and right plots of Figures 3.4 and 3.5.

The results for the two sources placed 80 cm apart are found in Figure 7.7. The results of the left source are plotted in red and for the right source in green. The large plot of Figure 7.7 gives an overview of the results for frequencies 100 - 10000 Hz. To have a closer look at the low frequency results, zoomed versions of the large plot are given in the two smaller plots. In the zoomed versions, only GO CSM and inverse SPI are plotted against the baseline. The results for the two sources placed 25 cm apart are found in Figure 7.8.

Figures 7.7 and 7.8 show that GO with the CSM energy function and inverse SPI give the best results for the experimental data. As one can see, for the two sources placed 25 cm apart, GO with the CSM energy function and inverse SPI give good agreement with the baseline from 600 Hz. For the two sources placed 80 cm apart there is already good agreement from 400 Hz. An explanation for this discrepancy is that the GO algorithm has more difficulty with the accurate identification of two closely spaced sources in comparison to two sound sources located further apart, as shown by the two bottom plots of Figure 6.3.

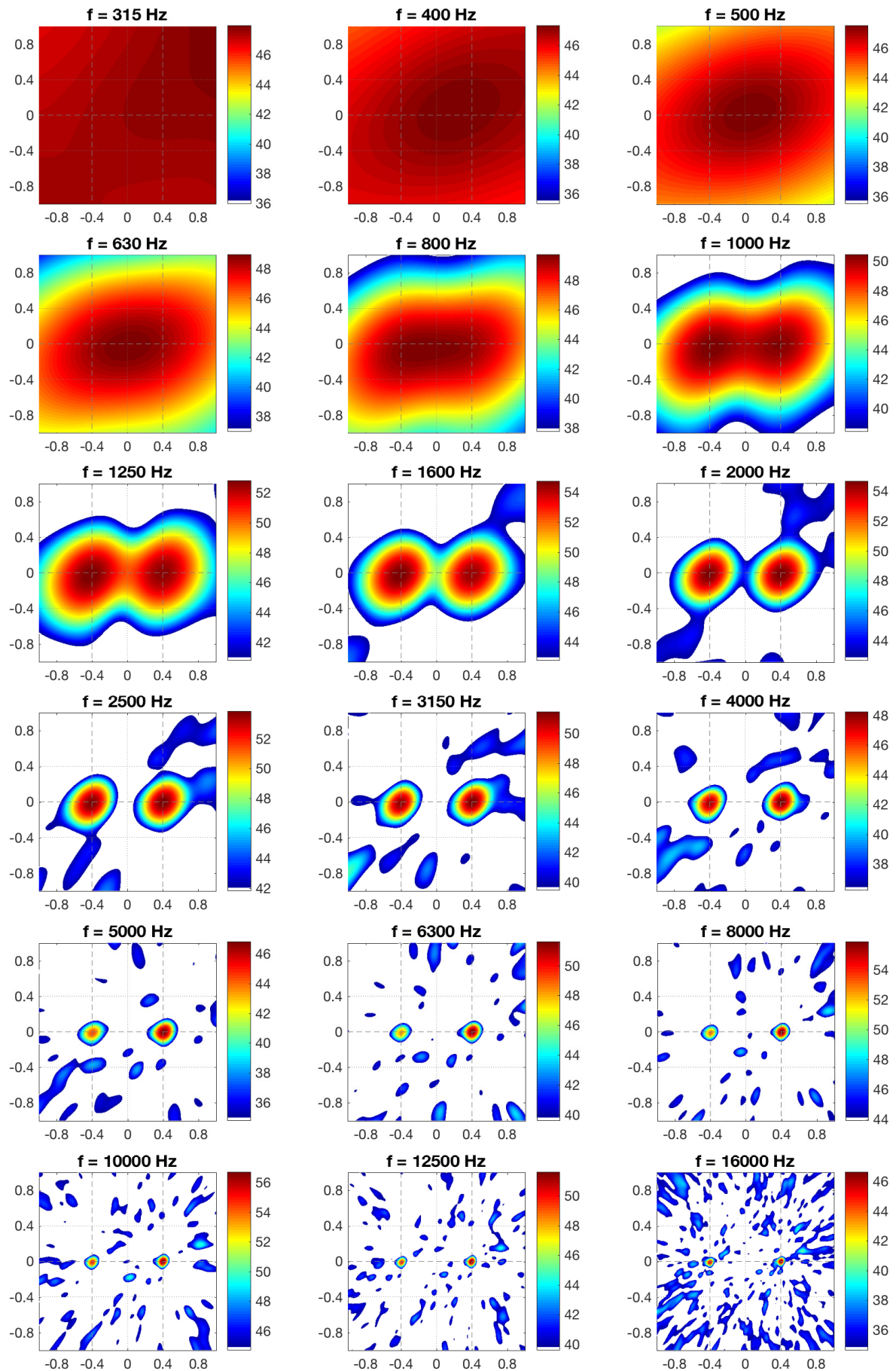


Figure 7.1: CB results summed over 1/3 octave bands for the experimental data set with two speakers broadcasting white noise, placed $\Delta x = 80$ cm apart.

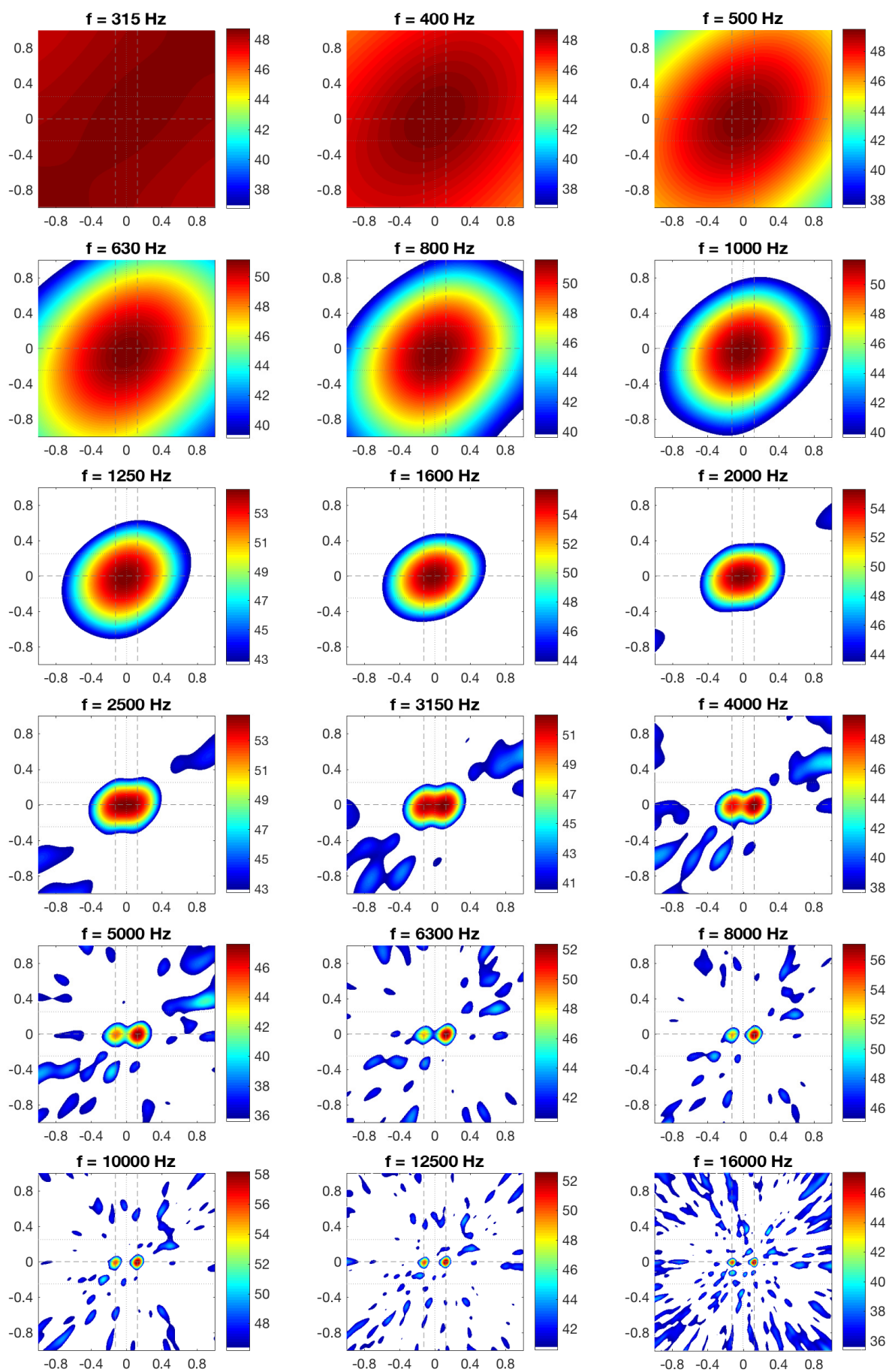


Figure 7.2: CB results summed over 1/3 octave bands for the experimental data set with two speakers broadcasting white noise, placed $\Delta x = 25$ cm apart.

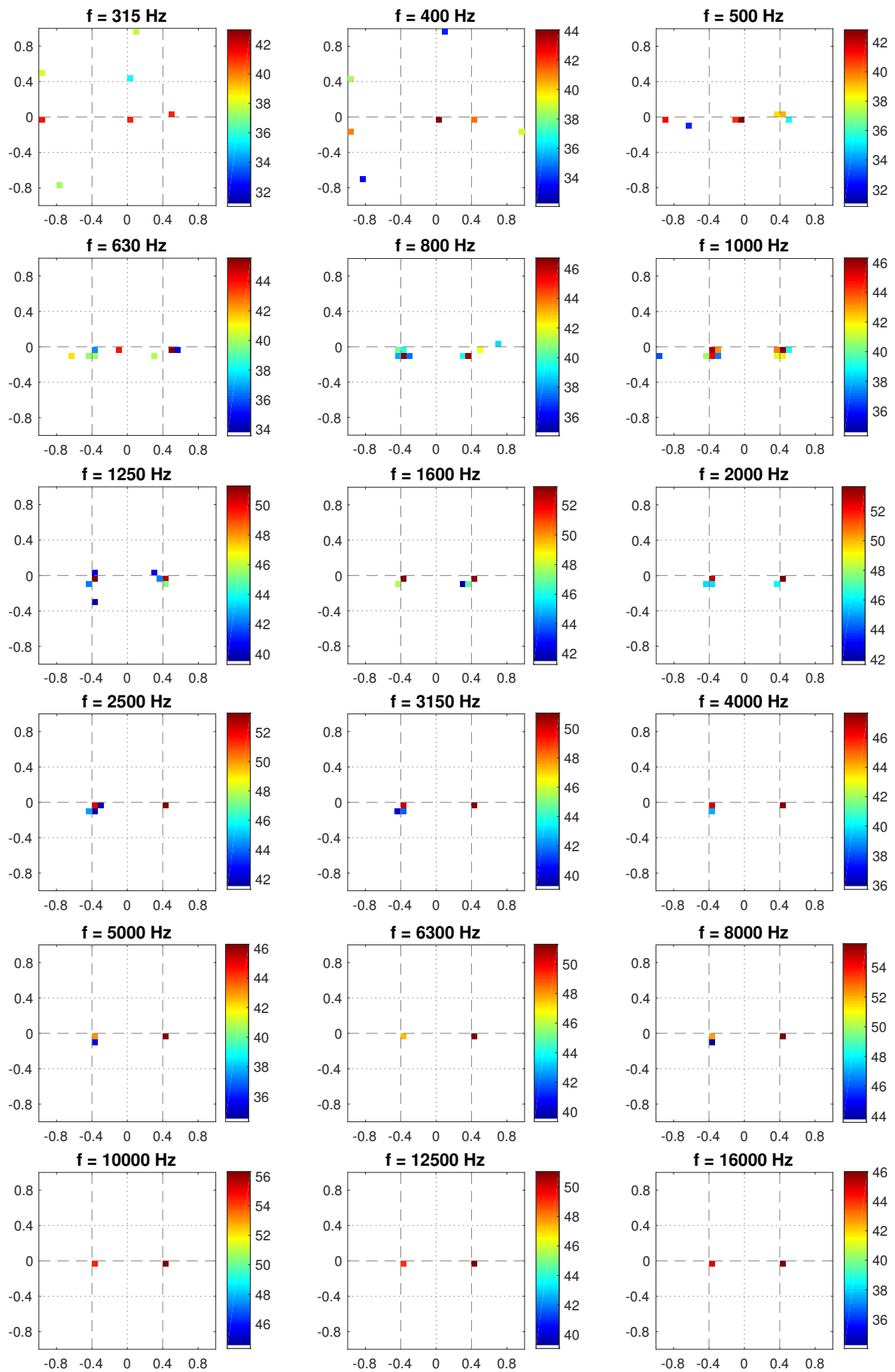


Figure 7.3: DAMAS results summed over 1/3 octave bands for the experimental data set with two speakers broadcasting white noise, placed $\Delta x = 80$ cm apart.

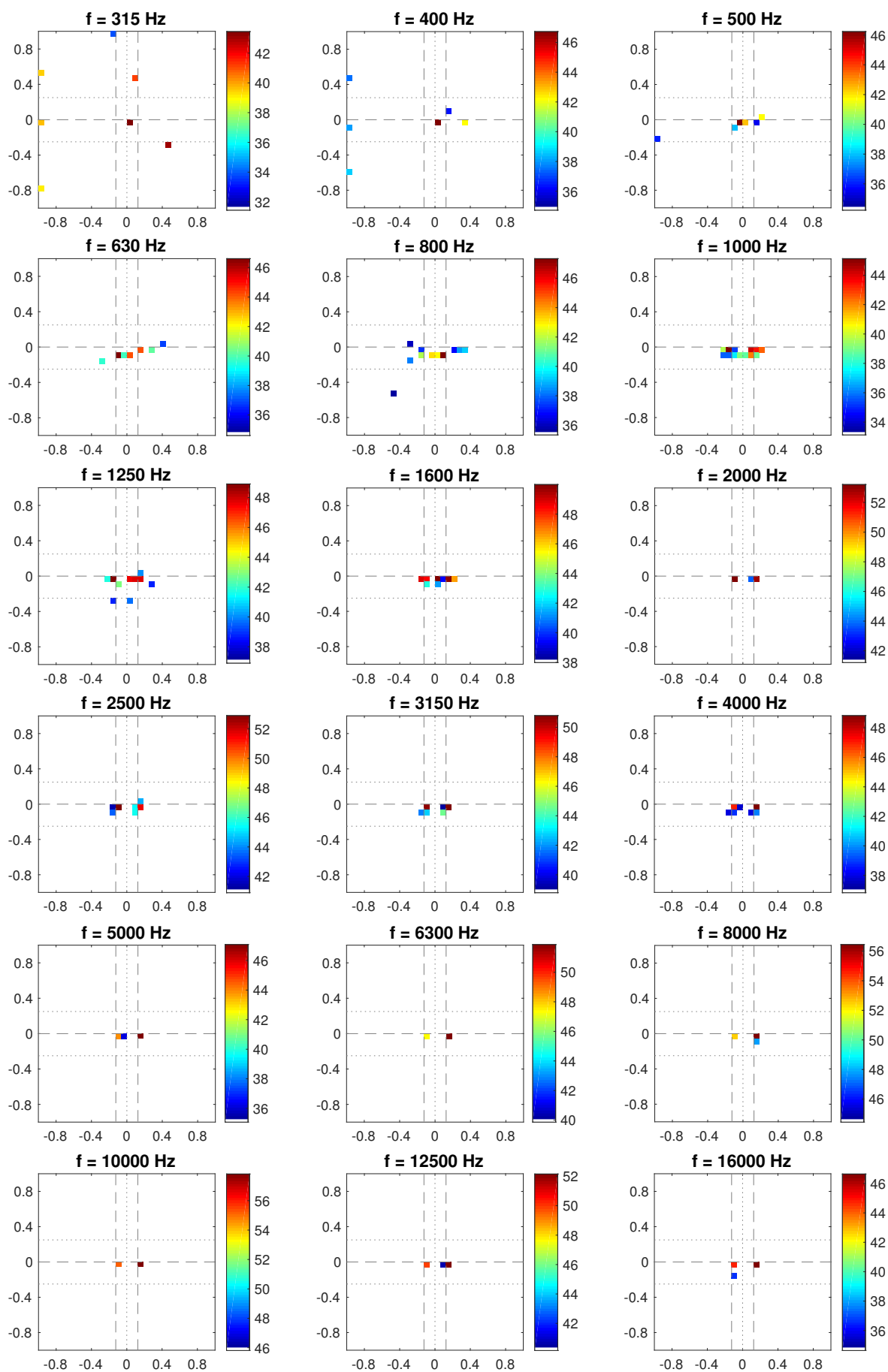


Figure 7.4: DAMAS results summed over 1/3 octave bands for the experimental data set with two speakers broadcasting white noise, placed $\Delta x = 25$ cm apart.

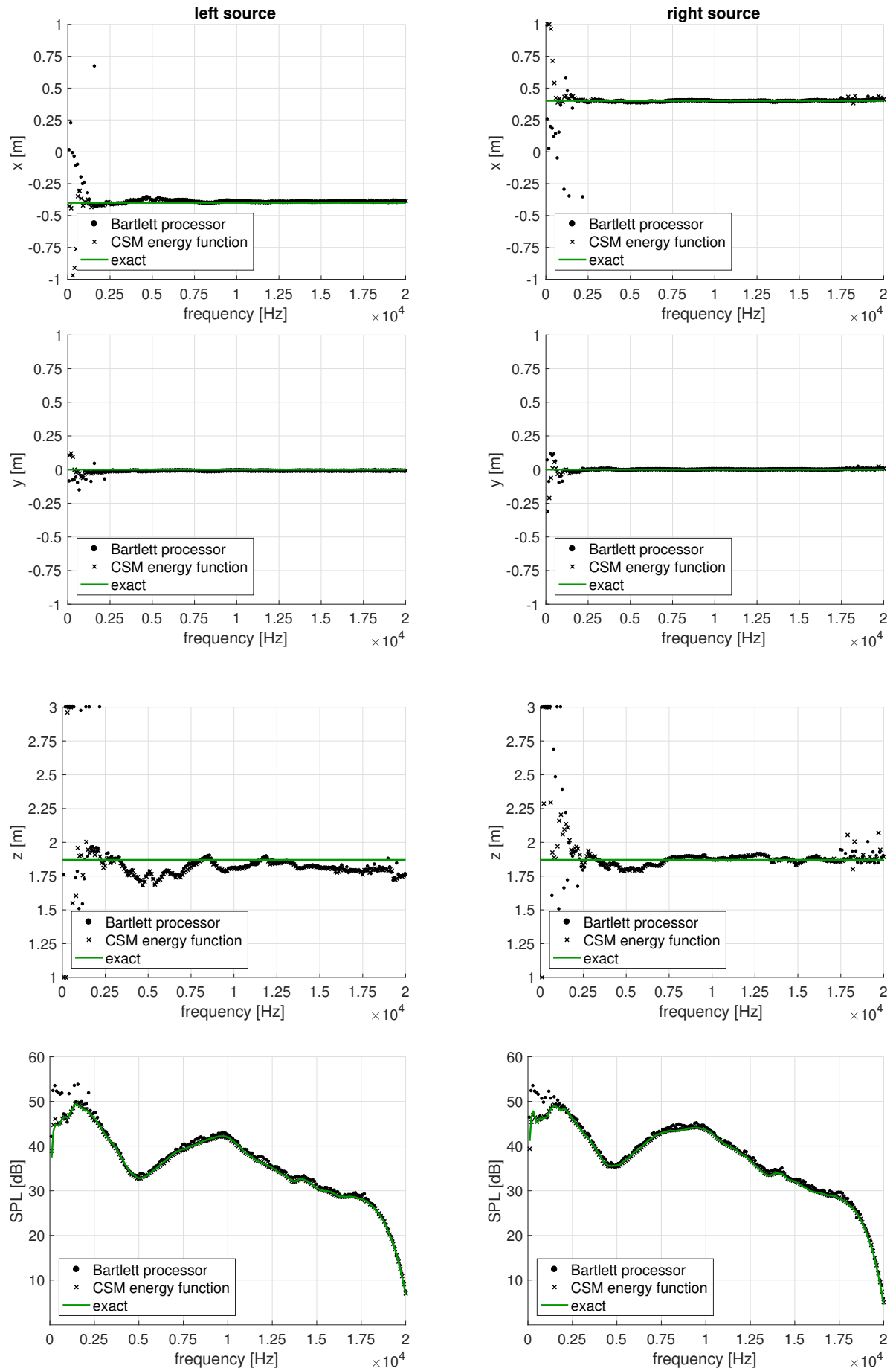


Figure 7.5: GO results for the experimental data set with two speakers broadcasting white noise, placed $\Delta x = 80$ cm apart. The green lines represent the exact source locations and SPLs.

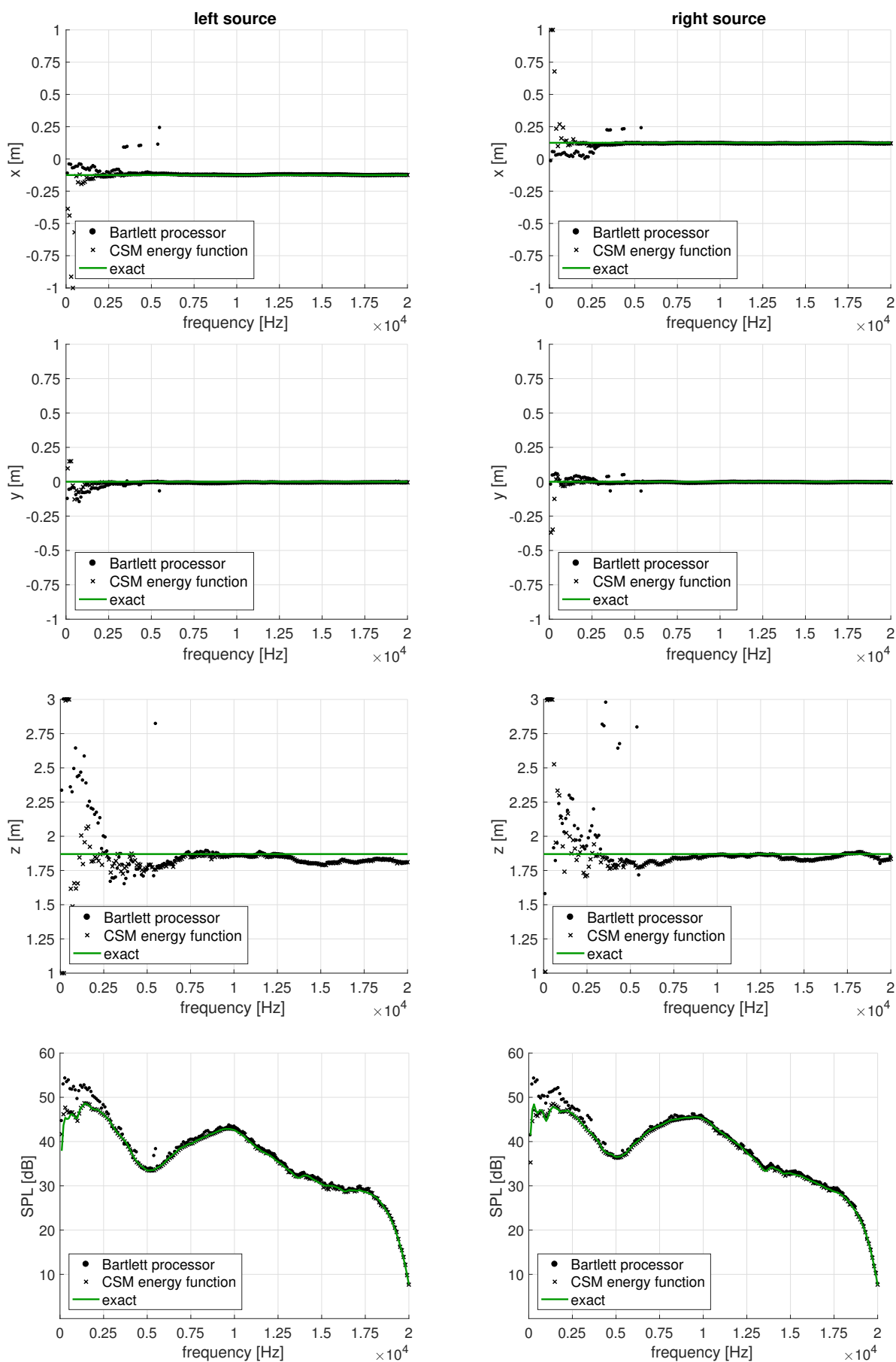


Figure 7.6: GO results for the experimental data set with two speakers broadcasting white noise, placed $\Delta x = 25$ cm apart. The green lines represent the exact source locations and SPLs.

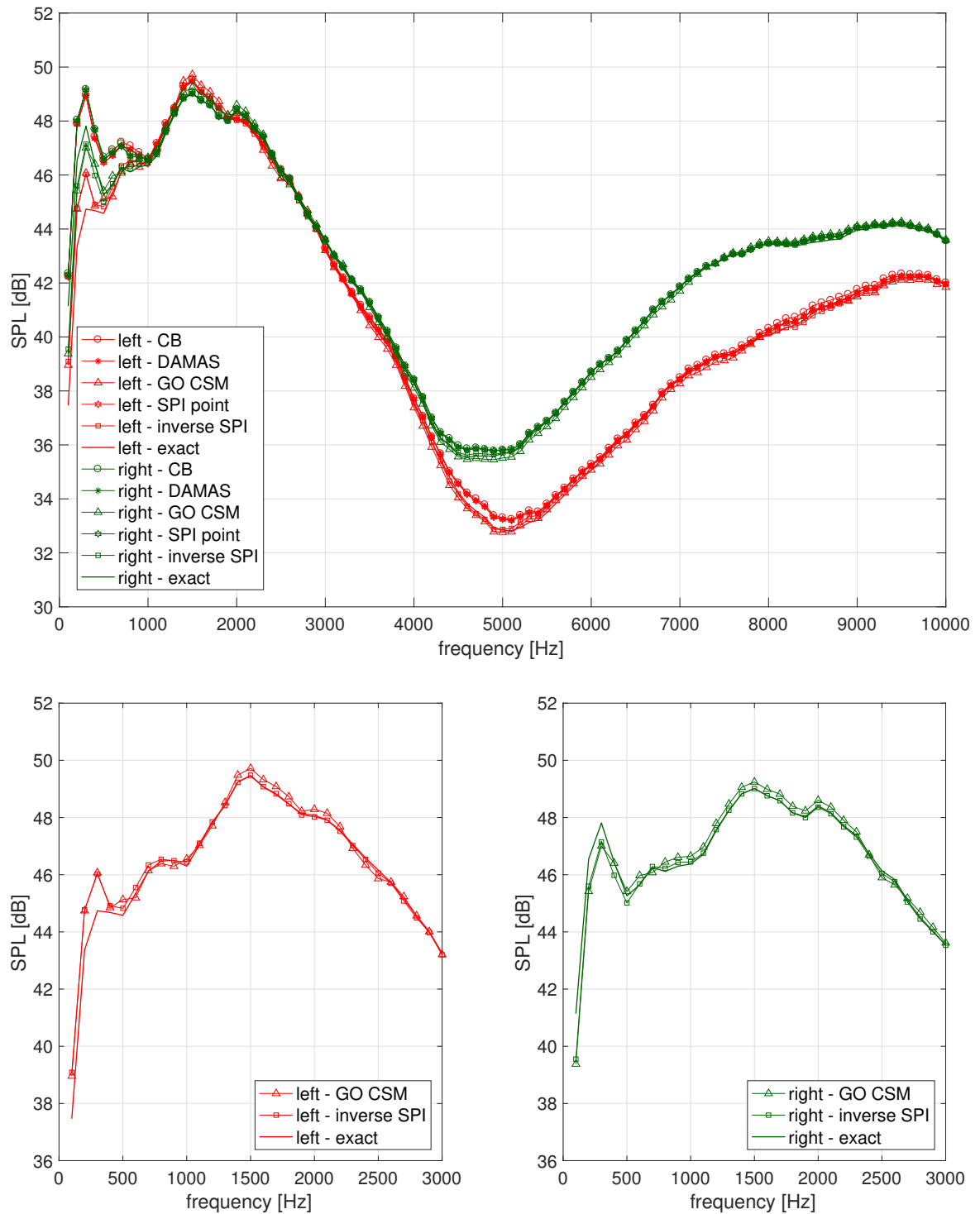


Figure 7.7: CB, DAMAS, GO and SPI results of two sound sources in the anechoic chamber, at 80 cm distance, compared against “exact” single speaker measurements, i.e. the baseline.

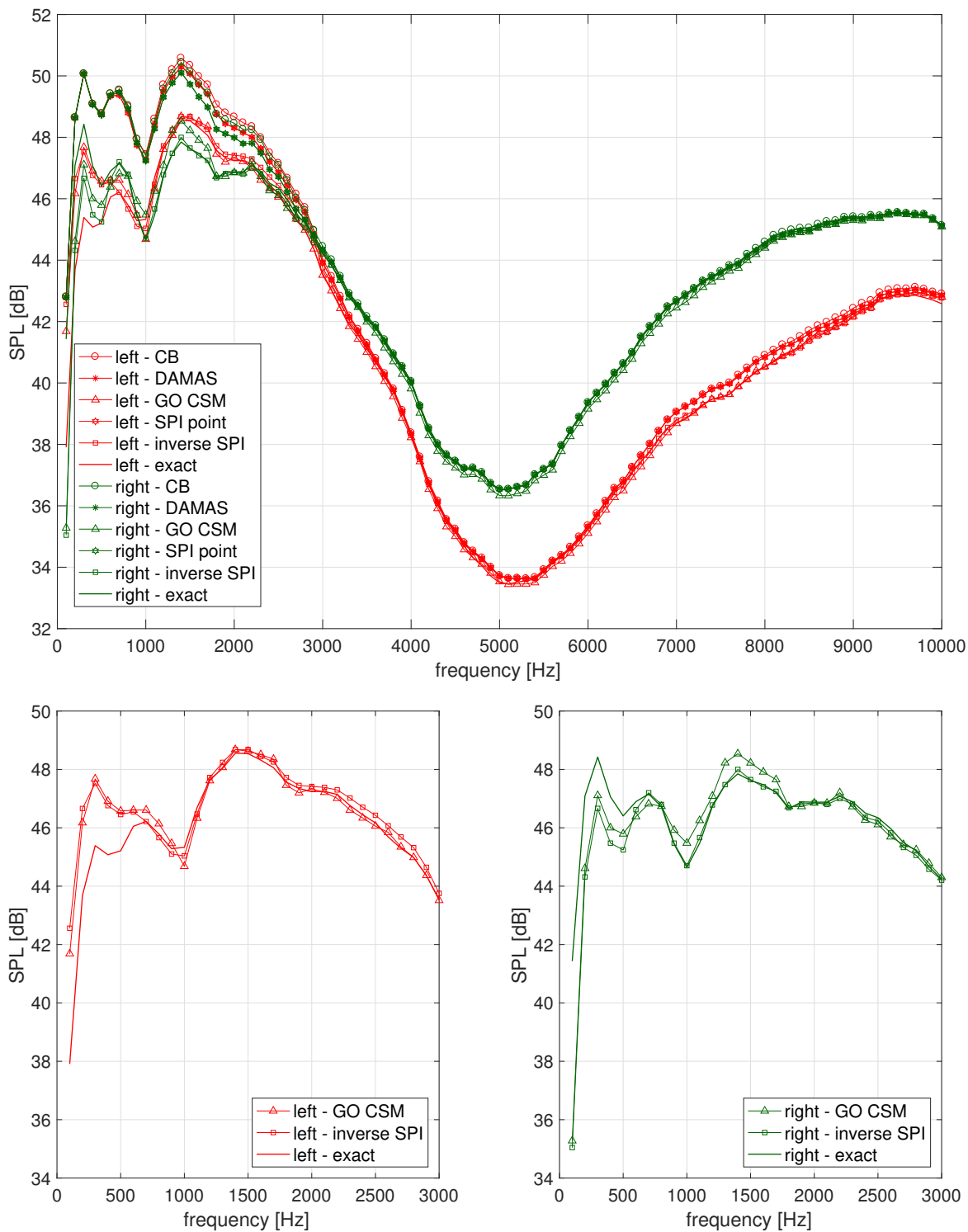
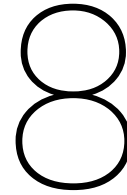


Figure 7.8: CB, DAMAS, GO and SPI results of two sound sources in the anechoic chamber, at 25 cm distance, compared against “exact” single speaker measurements, i.e. the baseline.



Conclusions and recommendations

Several conclusions are drawn from this research. The conclusions are discussed in Section 8.1 and the order in which the conclusions are given is: DAMAS - GO - SPI. Based on the conclusions, recommendations are made for future research in Section 8.2.

8.1. Conclusions

DAMAS, unlike CB, uses a model for multiple sources. DAMAS therefore adds value with regard to CB when applied to situations with multiple point sources present, potentially with varying source auto-powers. For CB, the stronger sources overshadow the weaker sources. The consequence is that the weaker sources are hidden behind side lobes. DAMAS is able to identify the sources in the correct source locations with the correct source auto-powers. This has been demonstrated with simulations and experimental data and applies to both separated point sources and distributed sources. The biggest disadvantage of DAMAS is its high computational demand.

GO with the Bartlett processor works perfectly for a single sound source. GO with the CSM energy function uses a model for multiple sources. Where GO with the Bartlett processor has difficulty with the accurate identification of two sound sources, especially at low frequencies, this is not a problem for GO CSM. The conclusions of the investigation of the performance of GO in identifying closely spaced sound sources from Chapter 6 are that GO CSM is perfectly capable of correctly locating sources far below the Rayleigh limit. Because GO CSM minimizes the difference between the measured and modeled CSM, noise distorts the operation of GO. In the presence of noise, removing the diagonal from the CSM improves the performance of GO. With sources of varying auto-powers and the presence of noise, GO is better able to localize the stronger source with respect to the weaker source. The closer the sound sources are spaced, the greater the improvement is that GO offers in the source localization compared to CB. GO finds the sources in three-dimensional space, i.e. it eliminates the need for defining a scan plane.

SPI is an algorithm that is able to quantify sound sources, but not to localize them. For the source localization another algorithm must be used, for example CB. SPI identifies source auto-powers for distributed sources more accurately and computationally more efficient than other acoustic imaging techniques. SPI point is a fast and effective algorithm for determining the OSPL of an integration area. It gives correct results for point sources and distributed sources built from point sources with equal source auto-powers. Inverse SPI performs simultaneous optimization, minimizing the difference between the CSM and the integration grids. This algorithm works well for distributed sources. For a distributed source built from point sources with varying source auto-powers, all other algorithms overestimate the source auto-power of the part with the weakest sources. Inverse SPI, on the other hand, yields very precisely the source auto-powers of the different parts, irrespective of the absolute value of the source auto-power.

This research concludes that GO is superior compared to other acoustic imaging techniques in locating and quantifying acoustic sources below the Rayleigh limit. This is both true from a spacing as frequency perspective. Lastly, this research concludes that SPI identifies source auto-powers for distributed sources more accurately and computationally more efficient than other acoustic imaging techniques.

8.2. Recommendations

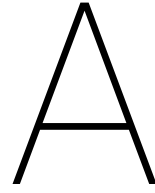
Given the promising results of GO CSM and inverse SPI, this research recommends researchers in the field of acoustic imaging to test the algorithms under additional circumstances. For example, it would be interesting to investigate the performance of inverse SPI with experimental data of distributed sources. Further, thus far GO was only tested on source data with source conditions which also could be located and quantified by acoustic imaging techniques that need a predefined scan grid. Testing GO under circumstances that align with its unique strength - namely the presence of multiple sound sources across three dimensions - would add value. If GO passes this test, this would negate the need to predefine, and consecutively scan, multiple two-dimensional scan grids. This would bring the field of acoustic imaging one step closer to the ultimate goal of real-time acoustic imaging across three dimensions.

Bibliography

- [1] Cover image, D. Palacios, "How does sound move? - Waves", URL: <https://danielpalacios.info/waves>, consulted 20–12–2017.
- [2] J.A. Hogbom, "Aperture Synthesis with a Non-Regular Distribution of Interferometer Baselines", *Astronomy and Astrophysics Supplement Series*, Vol. 15, June 1974, pp. 417–426.
- [3] T.J. Mueller, "Aeroacoustic Measurements", 1st ed., Springer-Verlag, Berlin, pp. 62–131, 2002.
- [4] Y. Liu, A. Quayle, A.P. Dowling, and P. Sijtsma, "Beamforming Correction for Dipole Measurement Using Two-Dimensional Microphone Arrays", *Journal of the Acoustical Society of America*, Vol. 124, No. 1, pp. 182–191, July 2008.
- [5] R.P. Dougherty, R.C. Ramachandran, and G. Raman, "Deconvolution of Sources in Aeroacoustic Images from Phased Microphone Arrays Using Linear Programming", *AIAA Paper 2013–2210*, May 2013.
- [6] P. Sijtsma, and R.W. Stoker, "Determination of Absolute Contributions of Aircraft Noise Components Using Fly-Over Array Measurements", *AIAA Paper 2004–2958*, 2004.
- [7] C. Camier, T. Padois, J. Provencher, P.A. Gauthier, A. Berry, J.F. Blais, M. Patenaude-Dufour, and R. Lapointe, "Fly-Over Source Localization on Civil Aircraft", *AIAA Paper 2013–2261*, May 2013.
- [8] U. Michel, B. Barsikow, J. Helbig, M. Hellmig, and M. Schüttpelz, "Flyover Noise Measurements on Landing Aircraft with a Microphone Array", *AIAA Paper 1998–2336*, 1998.
- [9] Y. Ishii, J. Hald, T. Ishii, H. Oinuma, K. Nagai, Y. Yokokawa, and K. Yamamoto, "High-Resolution Fly-Over Beamforming Using a Practical Array", *Berlin Beamforming Conference*, GfAI Gesellschaft zur Förderung angewandter Informatik e.V. Paper 2014–16, 2014.
- [10] P. Sijtsma, and H.M.M. van der Wal, "Identification of Noise Sources on Civil Aircraft in Approach Using a Phased Array of Microphones", *National Aerospace Lab. (NLR) TP–2004–166*, Amsterdam, The Netherlands, April 2004.
- [11] H.A. Siller, "Localisation of Sound Sources on Aircraft in Flight", *Berlin Beamforming Conference*, GfAI Gesellschaft zur Förderung angewandter Informatik e.V. Paper 2012–01, 2012.
- [12] G. Herold, and E. Sarradj, "Preliminary Benchmarking of Microphone Array Methods", *Berlin Beamforming Conference*, GfAI Gesellschaft zur Förderung angewandter Informatik e.V. Paper 2014–10, 2014.
- [13] G. Herold, and E. Sarradj, "An Approach to Estimate the Reliability of Microphone Array Methods", *AIAA Paper 2015–2977*, 2015.
- [14] P. Sijtsma, "Experimental Techniques for Identification and Characterisation of Noise Sources", *National Aerospace Lab. (NLR) TP–2004–165*, Amsterdam, The Netherlands, April 2004.
- [15] R. Merino-Martínez, M. Snellen, and D.G. Simons, "Functional Beamforming Applied to Imaging of Fly-over Noise on Landing Aircraft", *Journal of Aircraft*, Vol. 53, No. 6, November-December 2016.
- [16] R.P. Dougherty, "Functional Beamforming for Aeroacoustic Source Distributions", *AIAA Paper 2014–3066*, June 2014.
- [17] R.P. Dougherty, "Functional Beamforming", *Berlin Beamforming Conference*, GfAI Gesellschaft zur Förderung angewandter Informatik e.V. Paper 2014–01, 2014.
- [18] M. Dorigo, G. Di Caro, and L.M. Gambardella, "Ant algorithms for discrete optimization", *Artificial Life*, Vol. 5, No. 2, 1999, pp. 137–172.

- [19] M. Dorigo, V. Maniezzo, and A. Colorni, "Ant system: Optimization by a colony of cooperating agents", *IEEE Trans. Systems, Man, Cybernetics B*, Vol. 26, No. 1, 1996, pp. 29–41.
- [20] R. Storn, and K. Price, "Differential evolution — A simple and efficient heuristic for global optimization over continuous spaces", *J. Global Optim.*, Vol. 11, No. 4, 1997, pp. 341–359.
- [21] R. Storn, "On the usage of differential evolution for function optimization", *IEEE Biennial Conference of the North American Fuzzy Information Processing Society (NAFIPS)*, Berkeley, CA, 1996, pp. 519–523.
- [22] M. Snellen and D.G. Simons, "An assessment of the performance of global optimization methods for GEO-acoustic inversion", *J. Comput. Acoust.*, Vol. 16, No. 2, 2008, pp. 199–223.
- [23] P. Gerstoft, "Inversion of seismoacoustic data using genetic algorithms and a posteriori probability distributions", *J. Acoust. Soc. Am.*, Vol. 95, No. 2, 1994, pp. 770–782.
- [24] P. Sijtsma, "CLEAN Based on Spatial Source Coherence", *AIAA Paper 2007–3436*, 2007; also *National Aerospace Lab. (NLR) TP–2007–345*, Amsterdam, The Netherlands, December 2007.
- [25] J.J. Grefenstette, "Optimization of control parameters for genetic algorithms", *IEEE Trans. Systems, Man, Cybernetics A*, Vol. 16, No. 1, 1986, pp. 122–128.
- [26] C.E. Lindsay, and N.R. Chapman, "Matched-field inversion for geoacoustic model parameters using simulated annealing", *IEEE J. Ocean. Eng.* 18, 1993, pp. 224–231.
- [27] S. Kirkpatrick, C.D. Gelatt, and M.P. Vecchi, "Optimization by simulated annealing", *Science*, Vol. 220, No. 4598, 1983, pp. 671–680.
- [28] A.M.N. Malgoezar, M. Snellen, R. Merino-Martinez and D.G. Simons, "On the use of global optimization methods for acoustic source mapping", *Journal of the Acoustical Society of America*, Vol. 141, No. 1, January 2017, pp. 453–465.
- [29] F.R. Grosche, H. Stiewitt, and B. Binder, "Acoustic wind-tunnel measurements with a highly directional microphone", *AIAA Journal*, Vol. 15., No. 11, 1977, pp. 1590–1596.
- [30] R.H. Schlinker, "Airfoil trailing edge noise measurements with a directional microphone", *AIAA Paper 77-1269*, 1977.
- [31] S. Oerlemans, and P. Migliore, "Aeroacoustic Wind Tunnel Tests of Wind Turbine Airfoils", *AIAA Paper 2004–3042*, 2004.
- [32] T. Yardibi, J. Li, P. Stoica, N. Zawodny, and L. Cattafesta III, "A covariance fitting approach for correlated acoustic source mapping", *The Journal of the Acoustical Society of America*, Vol. 127, No. 5, May 2010, pp. 2920–2931.
- [33] S. Zhao, C. Tuna, and T.N.T. Nguyen, D.L. Jones, "Large-region acoustic source mapping using a movable array and sparse covariance fitting", *Acoustical Society of America*, Vol. 141, No. 1, January 2017, pp. 357–372.
- [34] P. Sijtsma, "Phased Array Beamforming Applied to Wind Tunnel and Fly-Over Tests", *National Aerospace Lab. (NLR) TP–2010–549*, Amsterdam, The Netherlands, December 2010.
- [35] T. Yardibi, J. Li, and P. Stoica, L. Cattafesta III, "Sparsity constrained deconvolution approaches for acoustic source mapping", *Acoustical Society of America*, Vol. 123, No. 5, May 2008, pp. 2631–2642.
- [36] E. Sarradj, "A fast signal subspace approach for the determination of absolute levels from phased microphone array measurements", *Journal of Sound and Vibration*, Vol. 329, No. 9, April 2010, pp. 1553–1569.
- [37] H. Cox, R.M. Zeskind, and M.M. Owen, "Robust Adaptive Beamforming", *IEEE Transactions on Acoustics, Speech and Signal Processing*, Vol. ASSP–35, No. 10, October 1987, pp. 1365–1376.
- [38] J. Li, P. Stoica, and Z. Wang, "On Robust Capon Beamforming and Diagonal Loading", *IEEE Transactions on Signal Processing*, Vol. 51, No. 7, July 2003, pp. 1702–1715.

-
- [39] X. Huang, L. Bai, I. Vinogradov, and E. Peers, "Adaptive Beamforming for Array Signal Processing in Aeroacoustic Measurements", *Journal of the Acoustical Society of America*, Vol. 131, No. 3, March 2012, pp. 2152–2161.
- [40] T.F. Brooks, and W.M. Humphreys, "A Deconvolution Approach for the Mapping of Acoustic Sources (DAMAS) Determined from Phased Microphone Arrays", *AIAA Paper 2004–2954*, 2004.
- [41] R.P. Dougherty, "Extensions of DAMAS and Benefits and Limitations of Deconvolution in Beamforming", *AIAA Paper 2005–2961*, May 2005.
- [42] T.F. Brooks, and W.M. Humphreys, "Extension of DAMAS Phased Array Processing for Spatial Coherence Determination (DAMAS-C)", *AIAA Paper 2006–2654*, May 2006.
- [43] T.F. Brooks, and W.M. Humphreys, "Three-Dimensional Application of DAMAS Methodology for Aeroacoustic Noise Source Definition", *AIAA Paper 2005–2960*, May 2005.
- [44] D.G. Simons, M. Snellen, B. Midden, M. Arntzen, and D.H.T. Bergmans, "Assessment of Noise Level Variations of Aircraft Flyovers Using Acoustic Arrays", *Journal of Aircraft*, Vol. 52, No. 5, September–October 2015, pp. 1625–1633.



Other beamforming methods

Functional Beamforming (FB) Side lobes (i.e. high beamforming output levels compared to the main lobe level, without the presence of a source) can be mistakenly interpreted as real sources. In order to suppress sidelobes, but to maintain correct source auto-powers, Dougherty developed the functional beamforming algorithm (FB) in 2014 [16, 17]. FB improves upon CB concerning the dynamic range and array spatial resolution.

CLEAN-PSF The CLEAN-PSF method [2, 24] starts with the dirty source map obtained by CB and cleans the source map in an iterative manner. Per iteration a scaled PSF is subtracted from the source map and replaced by a clean beam, i.e. a beam without side lobes. The iteration process goes on until a stop criterion is met.

CLEAN-SC The CLEAN-SC method [13, 24] performs the same steps as the CLEAN-PSF technique. The difference lies in the subtraction of the PSF belonging to the peak source location. The CLEAN-SC algorithm employs the fact that side lobes are coherent, see Section 2.3, with their main lobe in a source map. The iteration process goes on until a stop criterion is met.

Covariance Matrix Fitting (CMF) CMF [32] wants to approximate the measured CSM by minimizing the difference between a group of incoherent sources of equal source auto-power and the measured CSM with a least squares estimator. Variants of CMF exist, depending on the solution procedure. CMF works independently from beamforming methods, since it only solves a minimization problem. CMF is applied by various research groups, see [13, 33, 35].

Orthogonal Beamforming (OB) Orthogonal Beamforming [36] assumes that one eigenvalue of the CSM can be attributed to a sound source, incoherent with the other sources. The CSM is decomposed of its eigenvectors, which are orthogonal. With CB the source locations and auto-powers are calculated. One parameter has to be given in for OB, which is the number of eigenvalues assumed.

Robus Adaptive Beamforming (RAB) Robus Adaptive Beamforming [37] is also known as Capon beamforming. The objective of this method is to find the weight vector which maximizes the Signal Of Interest (SOI). To improve the robustness of RAB, Diagonal Loading (DL) [39] is applied. RAB is investigated by various research groups, see [15, 38].

B

DAMAS assumptions

DAMAS uses a model for multiple sources and assumes that the pressure vector \mathbf{p} is caused by K incoherent sources:

$$\mathbf{p} = \sum_{k=1}^K a_k \mathbf{g}_k \quad (\text{B.1})$$

In Equation B.1, \mathbf{p} is the pressure vector in [Pa], a_k is the complex pressure amplitude at grid point k and \mathbf{g}_k is the steering vector [-] towards grid point k .

The CSM is calculated by multiplying the pressure vector \mathbf{p} by its complex conjugate:

$$\tilde{\mathbf{C}} = \mathbf{p}\mathbf{p}^* = \left[\sum_j^K a_j \mathbf{g}_j \right] \left[\sum_k^K a_k^* \mathbf{g}_k^* \right] = \sum_{j,k} a_j a_k^* \mathbf{g}_j \mathbf{g}_k^* \quad (\text{B.2})$$

Applying averaging to obtain a time-averaged CSM, yields the following expression for the CSM $\tilde{\mathbf{C}}$:

$$\tilde{\mathbf{C}} = \sum_k^K |a_k|^2 \mathbf{g}_k \mathbf{g}_k^* = \sum_k^K A_k \mathbf{g}_k \mathbf{g}_k^* \quad (\text{B.3})$$

In Equation B.3, A_k is the source auto-power in [Pa²] at grid point k .